J. Fluid Mech. (1993), *vol.* 257, *pp.* 147–181

The final stage of the collapse of a cavitation bubble near a rigid wall

By SHEGUANG ZHANG[1], JAMES H. DUNCAN[1] AND GEORGES L. CHAHINE[2]

[1] Department of Mechanical Engineering, The University of Maryland, College Park, MD 20742, USA

[2] DYNAFLOW, Inc., 7210 Pindell School Road, Fulton, MD 20759, USA

(Received 17 November 1992 and in revised form 13 May 1993)

During the collapse of an initially spherical cavitation bubble near a rigid wall, a re-entrant jet forms from the side of the bubble farthest from the wall. This re-entrant jet impacts and penetrates the bubble surface closest to the wall during the final stage of the collapse. In the present paper, this phenomenon is modelled with potential flow theory, and a numerical approach based on conventional and hypersingular boundary integral equations is presented. The method allows for the continuous simulation of the bubble motion from growth to collapse and the impact and penetration of the re-entrant jet. The numerical investigations show that during penetration the bubble surface is transformed to a ring bubble that is smoothly attached to a vortex sheet. The velocity of the tip of the re-entrant jet is always directed toward the wall during penetration with a speed less than its speed before impact. A high-pressure region is created around the penetration interface. Theoretical analysis and numerical results show that the liquid–liquid impact causes a loss in the kinetic energy of the flow field. Variations in the initial distance from the bubble centre to the wall are found to cause large changes in the details of the flow field. No existing experimental data are available to make a direct comparison with the numerical predictions. However, the results obtained in this study agree qualitatively with experimental observations.

1. Introduction

Cavitation is an important engineering phenomenon that commonly occurs in fluid machinery, piping systems, liquid jets and a variety of boundary-layer flows. The major harmful effects of cavitation are erosion, noise and decrease in fluid-machinery efficiency (Hammitt 1980; Arndt 1981). In an effort to understand the fundamental physics of cavitation phenomena, a number of researchers have investigated the growth and collapse of individual bubbles near rigid boundaries. Experiments have been performed by Benjamin & Ellis (1966); Gibson (1968); Lauterborn & Bolle (1975); Chahine (1979, 1982); Gibson & Blake (1982); Tomita & Shima (1986); and Vogel, Lauterborn & Timm (1989). Using spark-generated or laser-generated cavitation bubbles and high-speed photographs it was found that, once generated, the bubble grows to a maximum size, and then starts to collapse, inducing a radial flow directed toward the bubble centroid. As the collapse proceeds, the surface of the bubble farthest from the wall moves much faster than the surface closer to the wall. This asymmetric motion creates a wall-directed re-entrant jet as the volume of the bubble decreases. Eventually, a liquid–liquid impact occurs between the front of the re-entrant jet and the

opposite side of the bubble. During this impact process, the jet penetrates the slower-moving fluid close to the wall.

Numerous theoretical and numerical studies of an individual bubble collapsing near a rigid boundary have also been made (see review articles by Prosperetti 1982; Blake & Gibson 1987). Because the available theoretical analysis is limited to asymptotic studies in which the deformation of the bubble is confined to a small perturbation range (Chahine 1982), numerical simulation has become an important tool for investigating the detailed physics of this phenomenon. Using a finite-difference approach, Plesset & Chapman (1971) conducted the first fully numerical study. Later, Mitchell & Hammitt (1973) used a modified Marker-and-Cell method to simulate similar cases. An approximate integral-equation approach was introduced by Bevir & Fielding (1974). In this work, sources and doublets were distributed along the axis of symmetry inside the bubble. Though this method requires less computational effort than the finite-difference method, it failed to simulate the formation of the re-entrant jet. Gibson & Blake (1980) and Blake & Gibson (1981) modified this method to study the bubble collapse near a rigid wall and a free surface. Based on Green's theorem and the direct boundary-integral approach, more detailed studies of cavitation bubbles near rigid boundaries have been presented by Guerri, Lucca & Prosperetti (1981); Cerone & Blake (1984); and Blake, Taib & Doherty (1986) for axisymmetric cases and by Chahine & Perdue (1988) and Chahine (1991) for three-dimensional cases. The numerical calculations of the migration of the bubble toward the rigid wall, the profiles of the bubble and the formation of the re-entrant jet were found to be in excellent agreement with experimental observations (Blake *et al.* 1986).

Once the re-entrant jet begins to penetrate the opposite side of the bubble, difficulties in experiments, theory and numerical calculations appear. Most experiments use photographs to track the bubble surface. Unfortunately, the jet impact process occurs inside a toroidal bubble and the images are consequently blurred and difficult to interpret. Theoretical analysis of the jet impact and penetration process is difficult because of the nonlinearity associated with the large motions of the bubble surface. Benjamin & Ellis (1966) postulated that upon jet impact the bubble must be transformed into a vortex ring bubble in order to conserve the Kelvin impulse of the flow. Several attempts have been made to simulate the jet impact and penetration processes numerically. Rogers *et al.* (1990) and Szymczak *et al.* (1993) have assumed an inviscid incompressible flow and used a finite-difference field approach. They demonstrated the capabilities of the method by simulating a single bubble collapse near a rigid wall including the impact of the re-entrant jet. Owing to limits in computing time and memory, the calculation was done at low resolution. It was therefore difficult to resolve the impact interface and there was a non-physical energy loss before impact. Attempts to use the direct boundary element method without modification to simulate the penetration process have failed. The failure is due to the inherent mathematical degeneracy of the conventional integral equation under this circumstance. In an effort to avoid this degeneracy problem, Best (1993) devised a two-phase procedure to carry out the calculations with the conventional boundary integral equation. The first phase includes the growth and collapse of the bubble up to the point in time when the north and the south poles of the bubble meet. Then, in the second phase, a ring bubble is assumed with a continuous velocity field everywhere in the fluid. The initial conditions for the ring bubble problem are based on the fluid motion just before impact and some *ad hoc* assumptions about the geometry of the ring bubble and the fluid velocity in the vicinity of the impact surfaces. The entire impact process occurs instantaneously in this

model. A similar two-phase method with a boundary integral approach was also reported by Lundgren & Mansour (1991) for the simulation of a vortex ring bubble.

In the present paper, the physics of cavitation bubbles is studied with a new boundary-integral technique that can compute the growth and collapse of the bubble including the impact and penetration of the re-entrant jet. This method allows for a continuous liquid–liquid impact as the two curved sides of the bubble collide, the penetration of the re-entrant jet into the fluid close to the wall and the formation of a shear layer along the impact interface. The physical and mathematical modelling of these processes is presented in §2. This modelling uses modified conventional and hypersingular boundary integral equations with non-regular boundaries to form a well-posed problem for times before and during jet impact and penetration. The details of the numerical scheme are discussed in §3. This scheme is verified and tested in §4 by computing static and dynamic problems with known solutions. The results of simulations are presented in §5. These results include velocity and pressure fields and bubble profiles. Calculations showing changes in the circulation and energy of the flow during jet impact and penetration are also computed and discussed in this section. The concluding remarks of this study are given in §6.

2. Mathematical formulation

2.1. *Physical assumptions, definitions and coordinates*

In the present paper, as well as numerous previously published studies of bubble collapse, the fluid motion is treated by potential theory. Viscous effects are neglected on the grounds that the timescale for viscous diffusion is much longer than the timesale for the collapse. Thus, the vorticity generated at the boundaries does not have sufficient time to diffuse into the flow. The extension of these studies to include the penetration phase of the motion does not alter this conclusion. In studies of bubble collapse before jet impact, the assumption of incompressibility has been made based on the idea that only a small fraction of the energy of the bubble motion is radiated away as sound. In the present case, the jet impact will cause an increase in the radiated sound; however, it will be shown that the potential flow model allows for the loss of energy due to impact. Surface tension effects are also neglected in the present calculations. Though the influence of surface tension grows as the bubble volume becomes very small, it has been shown that the inertia and pressure terms are still dominant (Hammitt 1980).

Profiles of a cavitation bubble just before the impact of the re-entrant jet and at a time later in the evolution of the bubble are shown in figures 1 (*a*) and 1 (*b*), respectively. These profiles are from the results of the present numerical model. From figure 1 (*a*), it can be seen that the radius of curvature at the north pole (N_p, defined as the point on the bubble axis that is farthest from the wall) is less than the radius of curvature at the south pole, S_p. Thus, the jet impact process begins with impact at a single point. This instant in time is defined as the initial impact. As the process continues, more and more of the two surfaces impact in a continuous manner and the bubble volume decreases. The fluid that was originally above the bubble in the figure penetrates into the fluid that is below the bubble creating the profile as shown in figure 1 (*b*). In a real flow, the interface between the fluid from above and below the bubble (called the impact or penetration interface in this paper) contains a mixture of gas, vapour and micro-bubbles, and a local shear layer is generated with the fluid in the jet moving toward the wall and the fluid outside the jet moving away from the wall. In the present potential flow approximation, the penetration interface is represented as a sheet with infinitesimal thickness. This sheet has the properties of a vortex sheet in that the

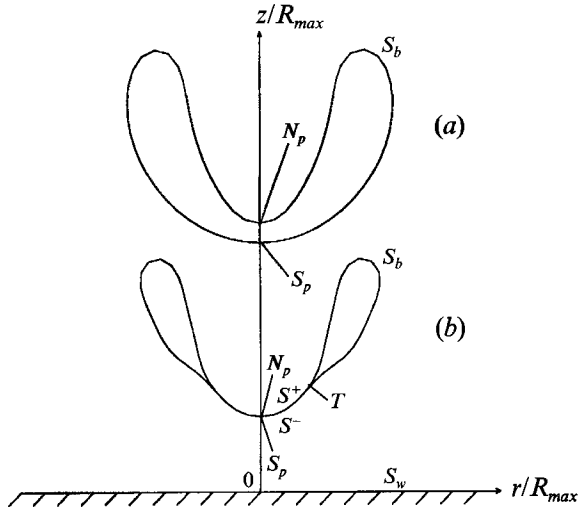

FIGURE 1. A cylindrical coordinate system and two axisymmetric bubble profiles corresponding to stages (*a*) before and (*b*) after penetration. The profiles have been separated vertically for clarity. S_b represents a regular surface, S^+ and S^- comprise a common surface which is connected to S_b at the triple point T, and S_w denotes an infinite rigid wall. N_p and S_p are respectively the north and south poles on the bubble surface.

pressure and normal velocities of the fluid are required to be continuous across the sheet while the tangential velocities are allowed to be discontinuous. The remainder of the bubble is toroidal in shape and is called a ring bubble. The circular line at which the vortex sheet attaches to the ring bubble is called the triple-point line and its intersection with the plane of the paper is denoted by the point T in figure 1(*b*). In the experiments, the ring-bubble contains some non-condensible gas which will cause the bubble to grow again after reaching a minimum volume. In the present model, the pressure in the bubble is assumed to be constant, therefore rebound will not occur. Current efforts are being directed toward simulating the rebound process with a volume-dependent pressure inside the bubble.

A cylindrical coordinate system is used to describe the motion of the fluid and bubble surface, with r, θ and z representing the radial, circumferential and axial coordinates, respectively. The fluid motion is assumed to be axisymmetric. A rigid wall is located in the plane $z = 0$ and extends to infinity. The pressure in the fluid far from the bubble, P_∞, is maintained constant as is the pressure in the bubble, P_0. Before initial impact, the bubble surface, as shown in figure 1(*a*), is entirely a regular surface (Kellogg 1953) and the fluid domain, D, is a simply connected region bounded by the bubble surface, S_b, the rigid wall, S_w, and an imaginary boundary at infinity, S_∞. After initial impact, S_b is transformed into an irregular surface as shown in figure 1(*b*). This surface consists of two different regions: a common surface region which comprises the two surfaces S^+ and S^-, representing the vortex sheet, and a regular surface region S_b which includes the ring bubble. The fluid domain is still simply connected when the internal boundary is taken as the union of S_b, S^+ and S^-.

The lengthscale for the problem is taken as R_{max} (the maximum radius the bubble would have achieved in an infinite fluid), the timescale is taken as $R_{max}[\rho/(P_\infty - P_0)]^{\frac{1}{2}}$ (the collapse time of a spherical bubble in an infinite fluid of density ρ), and the

pressure scale is $P_\infty - P_0 = \Delta P$. With respect to the three scaling parameters, the non-dimensionalized coordinates, r^* and z^*, time t^* and pressures P^* can be expressed as

$$\{r^*, z^*, t^*, P^*\} = \left\{\frac{r}{R_{max}}, \frac{z}{R_{max}}, \frac{t}{R_{max}}\left(\frac{\Delta P}{\rho}\right)^{\frac{1}{2}}, \frac{P}{\Delta P}\right\}. \tag{1}$$

Other geometric, kinematic and dynamic quantities in the following mathematical formulations are non-dimensionalized in the same manner. In the remainder of this paper, all variables are dimensionless and the superscript * is dropped for convenience.

2.2. *Mathematical statement of problem*

Based on potential flow theory, the velocity $\boldsymbol{u}$ can be represented by the gradient of the velocity potential $\phi, \boldsymbol{u} = \nabla\phi$, with ϕ satisfying Laplace's equation inside the fluid domain D,

$$\nabla^2\phi(\boldsymbol{x}, t) = 0, \quad \boldsymbol{x} \in D, \tag{2}$$

where $\boldsymbol{x}$ is the spatial coordinate. Initially, the bubble boundary is assumed to be a spherical surface with radius R_0. Over this surface, a uniformly distributed velocity potential ϕ is prescribed using Rayleigh's (1917) spherical bubble theory:

$$\phi_0 = -R_0\left[\frac{2\Delta P}{3\rho}\left(\frac{R_{max}^3}{R_0^3} - 1\right)\right]^{\frac{1}{2}}. \tag{3}$$

The boundary conditions before the impact of the re-entrant jet are as follows. The kinematic boundary condition on S_b is

$$\frac{\mathrm{d}\boldsymbol{x}_p}{\mathrm{d}t} = \nabla\phi, \quad \boldsymbol{x}_p \in S_b, \tag{4}$$

where $\boldsymbol{x}_p$ is the position vector to a material point $\boldsymbol{p}$. The kinematic boundary conditions on the rigid wall, S_w, and at infinity are, respectively,

$$\frac{\partial\phi}{\partial n} = 0, \tag{5}$$

and

$$|\nabla\phi| \to 0. \tag{6}$$

The dynamic boundary condition on S_b is

$$P(\boldsymbol{x}_p, t) = P_0, \quad \boldsymbol{x}_p \in S_b. \tag{7}$$

After initial impact, the boundary conditions (4) and (7) still apply without modification to fluid particles on S_b; however, matching conditions must be introduced on the common surface, $S^+ \cap S^-$. The component of the velocity normal to the common surface must be continuous across the surface,

$$\left.\frac{\partial\phi^+}{\partial n_p^+}\right|_{p\in S^+} = -\left.\frac{\partial\phi^-}{\partial n_p^-}\right|_{p\in S^-}, \tag{8}$$

where n_p^+ and n_p^- are outward normals (directed away from the fluid) to S^+ and S^- at $\boldsymbol{p}^+$ and $\boldsymbol{p}^-$, respectively. The pressure across the common surface must also be continuous,

$$P|_{p\in S^+} = P|_{p\in S^-}. \tag{9}$$

Note that the pressure varies along the common surface and is not in general equal to P_0.

In order to solve the problem, the dynamic boundary conditions on the bubble surface and the common surface, (7) and (9), must be written in terms of ϕ. On S_b, the condition on ϕ is Bernoulli's equation written in material derivative form:

$$\frac{\mathrm{D}\phi}{\mathrm{D}t} = \tfrac{1}{2}|\nabla\phi|^2 + \frac{P_\infty - P_0}{\rho}, \quad \boldsymbol{p} \in S_b. \tag{10}$$

To derive the equation for ϕ on the common surface, consider Bernoulli's equation written for p^+:

$$\frac{\partial\phi^+}{\partial t} + \left(\frac{\partial\phi^+}{\partial n^+}\right)^2 = \frac{1}{2}\left[\left(\frac{\partial\phi^+}{\partial n^+}\right)^2 - \left(\frac{\partial\phi^+}{\partial s^+}\right)^2\right] + \frac{P_\infty - P^+}{\rho}, \tag{11}$$

and for p^-:

$$\frac{\partial\phi^-}{\partial t} + \left(\frac{\partial\phi^-}{\partial n^-}\right)^2 = \frac{1}{2}\left[\left(\frac{\partial\phi^-}{\partial n^-}\right)^2 - \left(\frac{\partial\phi^-}{\partial s^-}\right)^2\right] + \frac{P_\infty - P^-}{\rho}. \tag{12}$$

The left-hand sides of these two equations are the time rates of change of ϕ following the component of the fluid motion in the direction normal to the common surface. After subtracting (12) from (11) and employing the matching conditions (8) and (9), the above equations become

$$\frac{\mathrm{D}(\phi^+ - \phi^-)}{\mathrm{D}_n t} = -\frac{1}{2}\left[\left(\frac{\partial\phi^+}{\partial s^+}\right)^2 - \left(\frac{\partial\phi^-}{\partial s^-}\right)^2\right], \tag{13}$$

where the subscript n indicates the derivative following the normal component of the flow.

2.3. *Conditions at the instant of impact*

As was pointed out in §2.1, the liquid–liquid impact occurs continuously. In the numerical model, this continuous impact will be simulated by a finite number of discrete impacts of surface panels of finite size. Each panel impact generates pressure impulses and, as is shown below, temporal discontinuities in ϕ and $\nabla\phi$ at the instant of the impact. The pressure impulse, I, is defined by

$$I = \lim_{t'' \to t'} \int_{t'}^{t''} P \,\mathrm{d}t, \tag{14}$$

where P is the impact pressure and t' and t'' represent the instants just before and just after the impact, respectively. Since the interval from t' to t'' is infinitesimal, it can be shown from Bernoulli's equation that the velocity potential and pressure impulse satisfy the following relation (Batchelor 1967):

$$\phi'' - \phi' = -I/\rho, \tag{15}$$

in which ϕ' and ϕ'' are, respectively, the velocity potentials just before and immediately after the impact. This equation states that whenever an impact occurs, the velocity potential is discontinuous at that instant and has a jump which is equal to $-I/\rho$. For any two impacting material points (p^+ and p^-) on the bubble surface, the above condition can be written as

$$\phi''^+(\boldsymbol{x}_{p^+}, t) = \phi'^+(\boldsymbol{x}_{p^+}, t) - I^+/\rho, \tag{16}$$

$$\phi''^-(\boldsymbol{x}_{p^-}, t) = \phi'^-(\boldsymbol{x}_{p^-}, t) - I^-/\rho. \tag{17}$$

Subtracting (17) from (16) and noting that I^+ is equal to I^- at the impact point, a relation for the difference in ϕ across the impact surface at the instant of impact is obtained,

$$\phi''^+(\boldsymbol{x}_{p^+}, t) - \phi''^-(\boldsymbol{x}_{p^-}, t) = \phi'^+(\boldsymbol{x}_{p^+}, t) - \phi'^-(\boldsymbol{x}_{p^-}, t). \tag{18}$$

This relation states that the difference in ϕ between two impacting points remains the same during the impact. In the present model, the difference in ϕ varies along the impact interface. Best (1993) derived the same relationship, but applied it only to the impact of the north and south poles. After impact, he created a simply connected fluid domain by using a fictitious cut along which the difference in ϕ was assumed constant.

2.4. *Boundary integral equations*

The initial boundary value problem for the velocity potential ϕ as defined in the previous subsections, is solved by the boundary integral equation method. For times before initial impact, the numerical solution method, which is explained in the following section, is the one used by Blake *et al.* (1986) and others. In this method, the boundary conditions, (4) and (10), are integrated over each time step to yield the new position of S_b and the value of ϕ on this surface. To proceed on to the next time step, the values of $\partial\phi/\partial n$ on S_b must be determined. This problem is solved with a well-known boundary integral representation derived from Green's theorem:

$$\int_{S_b \cup S_w} \left[G(\boldsymbol{p},\boldsymbol{q}) \frac{\partial \phi(\boldsymbol{q})}{\partial n_q} - \frac{\partial G(\boldsymbol{p},\boldsymbol{q})}{\partial n_q} \phi(\boldsymbol{q}) \right] \mathrm{d}S_q = \begin{cases} 2\pi\phi(\boldsymbol{p}), & \boldsymbol{p} \in S_b \cup S_w \\ 4\pi\phi(\boldsymbol{p}), & \boldsymbol{p} \in D, \end{cases} \tag{19}$$

where $\boldsymbol{p}$ is a field point, $\boldsymbol{q}$ is a source point varying as an integration variable on the surfaces $S_b \cup S_w$, $\mathrm{d}S_q$ is the differential area element of $S_b \cup S_w$, n_q is the normal to $S_b \cup S_w$ at $\boldsymbol{q}$ directed outward from the fluid and the kernel $G(\boldsymbol{p},\boldsymbol{q})$ is equal to $1/|\boldsymbol{p}-\boldsymbol{q}|$. Equation (19) is often called the conventional boundary integral equation (CBIE) in the sense that the kernels involved are weakly singular for $G(\boldsymbol{p},\boldsymbol{q})$ and Cauchy singular for $\partial G(\boldsymbol{p},\boldsymbol{q})/\partial n_q$, which are integrable without the need of any special treatment.

Unfortunately, the above approach fails when the re-entrant jet approaches the opposite surface of the bubble in the final stage of the collapse. This failure is caused by two problems with the CBIE. First, just before initial impact, an equation written for a point on the tip of the re-entrant jet will be nearly identical to that written for a corresponding point near the south pole of the bubble. Thus, for instance, if one is solving for $\partial\phi/\partial n$ with known ϕ, an ill-conditioned or nearly singular coefficient matrix will result in the boundary element calculations. Second, just after initial impact, due to the matching condition (8) the integral of $\partial\phi/\partial n$ along S^+ and S^- will cancel. Thus, additional equations are needed to calculate $\partial\phi/\partial n$ along the common surface. In the following, a new approach is presented in which the CBIE is modified to account for the common surface and a hypersingular boundary integral equation (HBIE) is introduced to form a closed equation system. With this new approach, the calculations based on the boundary integral equation method can be carried out continuously from before initial impact into the penetration process.

Making use of the properties of single- and double-layer potentials (Günter 1967; Burton & Miller 1971) as well as the matching condition (8), the CBIE (19) is modified in Appendix A for cases with a common surface to yield

$$\int_{S_b \cup S_w} \left[G(\boldsymbol{p},\boldsymbol{q}) \frac{\partial \phi(\boldsymbol{q})}{\partial n_q} - \frac{\partial G(\boldsymbol{p},\boldsymbol{q})}{\partial n_q} \phi(\boldsymbol{q}) \right] \mathrm{d}S_q - \int_{S^+} \frac{\partial G(\boldsymbol{p},\boldsymbol{q})}{\partial n_q^+} [\phi^+(\boldsymbol{q}) - \phi^-(\boldsymbol{q})] \, \mathrm{d}S_q^+ = \begin{cases} 2\pi\phi(\boldsymbol{p}), & \boldsymbol{p} \in S_b \cup S_w \\ 2\pi[\phi^+(\boldsymbol{p}) + \phi^-(\boldsymbol{p})], & \boldsymbol{p} \in S^+ \end{cases}. \tag{20}$$

In this modified CBIE, the equation is written with respect to $\boldsymbol{p} \in S^+$ when the field point $\boldsymbol{p}$ is on the common surface $S^+ \cap S^-$. In the following section, on the numerical technique, it will be shown that during penetration the boundary conditions can be

integrated over each time step to yield the new positions of the surfaces S_b and $S^+ \cap S^-$, the values of ϕ on S_b and the values of $\phi^+ - \phi^-$ on $S^+ \cap S^-$. With these values, $\partial\phi/\partial n$ on S_b and $\phi^+ + \phi^-$ on $S^+ \cap S^-$ can be determined from (20). However, $\partial\phi/\partial n$ on the sheet is still unknown.

In order to find an analytical expression for $\partial\phi/\partial n$ on the common surface, the modified HBIE is derived in Appendix A by performing a directional derivative of the CBIE with $\boldsymbol{p}$ inside the domain D and then letting $\boldsymbol{p}$ approach the boundary along a direction normal to the boundary. The expression of the modified HBIE has the form

$$\int_{S_b \cup S_w} \left[\frac{\partial G(\boldsymbol{p},\boldsymbol{q})}{\partial n_p} \frac{\partial \phi(\boldsymbol{q})}{\partial n_q} - \frac{\partial^2 G(\boldsymbol{p},\boldsymbol{q})}{\partial n_p \partial n_q} \phi(\boldsymbol{q}) \right] \mathrm{d}S_q - \int_{S^+} \frac{\partial^2 G(\boldsymbol{p},\boldsymbol{q})}{\partial n_p \partial n_q} [\phi^+(\boldsymbol{q}) - \phi^-(\boldsymbol{q})] \, \mathrm{d}S_q^+ = \begin{cases} 2\pi \, \partial\phi(\boldsymbol{p})/\partial n_p, & \boldsymbol{p} \in S_b \cup S_w \\ 4\pi \, \partial\phi^+(\boldsymbol{p})/\partial n_p^+, & \boldsymbol{p} \in S^+ \end{cases}, \quad (21)$$

where n_p is the outward normal of the surface at $\boldsymbol{p}$. Like (20), this modified HBIE is valid for the field point $\boldsymbol{p}$ either on the common surface or on the rest of the boundaries. From (21), $\partial\phi/\partial n$ on both $S^+ \cap S^-$ and S_b can be determined as long as ϕ on the surfaces $S_b \cup S_w$ and $\phi^+ - \phi^-$ on S^+ are prescribed.

2.5. *Energy considerations*

The equation governing the energy of the flow is

$$\int_{V_f(t)} \tfrac{1}{2} q^2 \, \mathrm{d}V - \int_{V_f(0)} \tfrac{1}{2} q^2 \, \mathrm{d}V + \frac{P_\infty - P_0}{\rho} (V_b(t) - V_b(0)) = 0, \quad (22)$$

where the integration limits $V_f(t)$ and $V_f(0)$ are the fluid volumes at times t and $t = 0$, respectively, and $V_b(t)$ and $V_b(0)$ are the volumes of the bubble at times t and $t = 0$, respectively (see Duncan & Zhang 1991, equation (12)). The first two terms on the left are the kinetic energies of the fluid at the two times and can be calculated from surface integrals over the bubble and the common surface (Lamb 1945):

$$\int_{V_f(t)} \tfrac{1}{2} q^2 \, \mathrm{d}V = \frac{1}{2} \int_S \phi \frac{\partial \phi}{\partial n} \mathrm{d}s, \quad (23)$$

where S is the internal boundary $S_b \cup S^+ \cup S^-$. The third term in (22) is the potential energy defined as the work done against the pressure at infinity due to changes in the bubble volume.

For times up to the instant before initial impact, the total energy of the system is constant. During the collapse phase before impact, the potential energy decreases and the kinetic energy increases by equal amounts. However, there is a loss of kinetic energy associated with the liquid–liquid impact and this energy is not converted to potential energy. Thus, the total energy decreases. This kinetic energy loss is given by the following equation which is derived in Appendix B:

$$\Delta E_k = \int_D \tfrac{1}{2}\rho(\nabla\phi'')^2 - \tfrac{1}{2}\rho(\nabla\phi')^2 \, \mathrm{d}V = -\frac{1}{2} \int_{S^+} I^+ (\nabla(\phi')^+ - \nabla(\phi')^-) \cdot \boldsymbol{n}_+ \, \mathrm{d}S. \quad (24)$$

Rogers *et al.* (1990) and Szymczak *et al.* (1993) also noted an energy loss during impact and presented a similar formula. In the above equation, the value of I^+ is a positive maximum at the impact interface since the gradient of I must accelerate the fluid on both sides of the interface in directions away from the interface. The difference in the normal components of the velocities inside the brackets is always positive as long as there is an impact. Thus, ΔE_k must be less than zero. It should be noted that the above

expression was derived on the assumption that the colliding surfaces stick together after impact. It is this assumption that causes the loss in energy.

As an example of a simple impact problem demonstrating the energy loss, consider two parallel liquid layers of infinite extent in planes normal to the z-axis. One layer is above the $z = 0$ plane and has a uniform velocity $v = -V\hat{k}$ and a thickness h^+ while the other layer is below the plane $z = 0$ and has a uniform velocity $v = V\hat{k}$ and a thickness h^-. Impact occurs when the 'inner' surfaces meet at $z = 0$. In this example, the divergence of equation (B 1) yields

$$\frac{\partial^2 I}{\partial z^2} = -2\rho V\delta(z), \tag{25}$$

which has the solution

$$I^+ = \frac{-2\rho V h^-}{h^+ + h^-}(z - h^+) \tag{26}$$

in the upper layer. Evaluation of (24) in this case yields

$$\Delta E_k = 2\rho V^2 \frac{h^+ h^-}{h^+ + h^-} \tag{27}$$

per unit area. Thus, for the case when $h^+ = h^- = H$, the kinetic energy change is $-\rho V^2 H$ per unit area. This change is equal to the total kinetic energy before impact and indicates that, as expected, the two layers will come to rest after impact.

3. Numerical scheme

The numerical schemes to be discussed in this section deal with two issues: the accurate solution of the integral equation system (20) and (21) at a given time instant and the time advancement of the boundary conditions (4), (10) and (13). For the first issue, it is important to note that while the introduction of the modified HBIE (21) produces a well-posed system of equations during penetration, it unfortunately makes the numerical scheme more complicated than schemes that use the CBIE alone in cases before penetration. These complications arise out of the need for regularizing the hypersingular kernel, making the solutions unique and discretizing the geometry and density functions properly. For the second issue, the kinematic boundary condition must be modified slightly to treat the node points on the vortex sheet.

3.1. *Regularization of the hypersingular integral*

As can be seen from (21), the kernel $\partial^2 G(\boldsymbol{p}, \boldsymbol{q})/\partial n_p \partial n_q$ has a third-order singularity $(1/|\boldsymbol{p} - \boldsymbol{q}|^3)$ as $\boldsymbol{p}$ approaches $\boldsymbol{q}$, which makes it non-integrable in the ordinary sense. Several regularization techniques to treat integrals of this kind exist (Meyer, Bell & Zinn 1978; Ingber & Rudolph 1990; Krishnasamy *et al.* 1990). In this paper, the hypersingular kernel has been transformed to a Cauchy-singular kernel. The relation between the two kernels can be expressed in the identity (Ingber & Rudolph 1990)

$$\int_S \phi(\boldsymbol{q}) \frac{\partial^2 G(\boldsymbol{p}, \boldsymbol{q})}{\partial n_p \partial n_q} \mathrm{d}S_q = \int_S [\boldsymbol{n}_q \times \nabla_q \phi(\boldsymbol{q})] \cdot [\boldsymbol{n}_p \times \nabla_p G(\boldsymbol{p}, \boldsymbol{q})] \mathrm{d}S_q, \tag{28}$$

where the gradient operator with a subscript indicates that the operation is carried out with that subscript as a variable. The decomposition of this integral in a cylindrical coordinate system with axisymmetry transforms the density function $\phi(\boldsymbol{q})$ in (28) to the density function $\partial\phi(\boldsymbol{q})/\partial s_q$, where s_q is the arclength along the surface. The corresponding derivations related to this decomposition and expressions for other terms in (21) can be found in Appendix C.

3.2. *Uniqueness of solutions of the hypersingular integral equation*

Using the hypersingular integral equation (21) alone to solve the Dirichlet problem of Laplace's equation will result in non-unique solutions. (Solutions are only unique up to an additive constant.) This non-uniqueness can be easily deduced from the identity (28) in that, if $\phi(q)$ is a constant along the surface, the integral with the hypersingular kernel is identically equal to zero; thus, (21) will yield $\partial\phi/\partial n = 0$ at all points on the surface. However, this contradicts the well-known case of a Rayleigh spherical bubble in an infinite fluid where a uniformly distributed ϕ on the bubble corresponds to a non-zero $\partial\phi/\partial n$ on the surface. In the present work, this non-uniqueness is resolved by introducing a combined scheme in which the modified CBIE and HBIE are jointly used. In this combined scheme, the CBIE is responsible for recovering the constant in ϕ along the surface which would be lost if the HBIE were used alone.

3.3. *Time advancement algorithm*

The time advancement techniques for times before and during penetration are discussed separately in this subsection. All of the temporal integrations are performed by the following predictor-corrector scheme. Given an ordinary differential equation $dy/dt = f(t, y)$ with an initial condition $y(t_0) = y_0$, the numerical solution for y at step $i+1$ $(i = 0, 1, \ldots)$ is given by

predictor step: $$y^*_{i+1} = y_i + (t_{i+1} - t_i) f(t_i, y_i), \tag{29}$$

corrector step: $$y_{i+1} = y_i + \tfrac{1}{2}(t_{i+1} - t_i)[f(t_i, y_i) + f(t_{i+1}, y^*_{i+1})]. \tag{30}$$

For ease of presentation, only the predictor step is presented in the following.

3.3.1. *Time marching before initial impact*

Let us assume that at time t all quantities are known. To proceed on to $t+\Delta t$, the boundary conditions (4) and (10) are integrated following the fluid particle $\boldsymbol{p}$ on the surface S_b:

$$\boldsymbol{x}_p(t+\Delta t) = \boldsymbol{x}_p(t) + \nabla\phi(\boldsymbol{x}_p, t)\,\Delta t, \tag{31}$$

$$\phi(\boldsymbol{x}_p, t+\Delta t) = \phi(\boldsymbol{x}_p, t) + \Delta t\left(\frac{|\nabla\phi(\boldsymbol{x}_p, t)|^2}{2} + \frac{P_\infty - P_0}{\rho}\right). \tag{32}$$

These equations yield the new position of S_b and the values of ϕ on this surface at $t+\Delta t$. From this information, the derivative of ϕ in the direction tangent to the surface can be computed. In order to proceed to integrate (4) and (10) over the next time step the values of $\partial\phi/\partial n$ are required. These values are obtained by solving the integral equations.

3.3.2. *Time marching after initial impact*

After initial impact, material points on the toroidal bubble are treated like those before impact by integrating (4) and (10). The integration of the boundary conditions for points on the common surface is somewhat more complicated since two fluid particles, $\boldsymbol{p}^+$ on S^+ and $\boldsymbol{p}^-$ on S^-, occupying the same location on each side of the surface at time t will in general not be together at the next time step (the tangential velocities are not equal on each side of the sheet). The relation between the velocity of a fluid particle $\boldsymbol{p}$ and the velocity of its projection in the direction normal to the surface is

$$\left(\frac{d\boldsymbol{x}^n_p}{dt}\cdot\boldsymbol{n}_p\right)\boldsymbol{n}_p = \frac{\partial\phi}{\partial n}\boldsymbol{n}_p = \frac{d\boldsymbol{x}^n_p}{dt}, \tag{33}$$

where $\boldsymbol{x}_p^n$ is the position vector of the projection of $\boldsymbol{x}_p$ in the normal direction $\boldsymbol{n}_p$. Writing this relation at $\boldsymbol{p}^+$ and $\boldsymbol{p}^-$ on S^+ and S^- for the predictor step yields

$$\boldsymbol{x}_{p^+}^n(t+\Delta t) = \boldsymbol{x}_{p^+}^n(t)+\Delta t\frac{\partial\phi^+}{\partial n_p^+}\boldsymbol{n}_p^+, \tag{34}$$

and

$$\boldsymbol{x}_{p^-}^n(t+\Delta t) = \boldsymbol{x}_{p^-}^n(t)+\Delta t\frac{\partial\phi^-}{\partial n_p^-}\boldsymbol{n}_p^-, \tag{35}$$

respectively. In view of the matching conditions (8) and the fact that $\boldsymbol{n}_p^+ = -\boldsymbol{n}_p^-$, the above equations reduce to a single equation yielding the new position of the common surface at time $t+\Delta t$. The boundary condition (13) integrated for the predictor step is

$$\phi_n^+(t+\Delta t)-\phi_n^-(t+\Delta t) = \phi_n^+(t)-\phi_n^-(t)-\frac{\Delta t}{2}\left[\left(\frac{\partial\phi^+}{\partial s^+}\right)^2-\left(\frac{\partial\phi^-}{\partial s^-}\right)^2\right], \tag{36}$$

where the subscript n indicates the values of ϕ at a point following the normal flow.

It should be emphasized that it is the values of ϕ on the bubble surface (S_b) and the values of $\Delta\phi(=\phi^+-\phi^-)$ on the impact interface ($S^+\cap S^-$) that are advanced in time by (32) and (36). Both quantities are continuous with respect to time.

3.3.3. *Time step determination*

In the time advancement, a variable time step technique is adopted. At each step, the time increment Δt is determined by

$$\Delta t = \frac{C}{1+0.5V_{max}^2}, \tag{37}$$

where V_{max} is the maximum velocity on the bubble surface at the current time step and C is a constant that is taken as 0.04 before penetration when the CBIE is used and 0.01 during penetration when the combined scheme is employed. The determination of these values of C is explored in §4.3.

3.4. *Numerical implementation of the integral equations*

The modified CBIE (20) and HBIE (21) are solved by the boundary element method. The infinite rigid wall is simulated by an image bubble. The bubble surface is discretized by n_b panels. Given the r- and z-coordinates of n_b+1 panel nodes along the surface, the coordinates r and z along each panel can be written as functions of a cubic spline parameter, ζ, which is chosen as a variable along the chord length of each panel (Dommermuth & Yue 1987; and Press *et al.* 1989),

$$r = r(\zeta), \quad z = z(\zeta). \tag{38}$$

Thus, the arclength coordinate, s, along each panel can be calculated by

$$s(\zeta) = \int_0^s \mathrm{d}s = \int_0^\zeta\left[\left(\frac{\mathrm{d}r}{\mathrm{d}\zeta}\right)^2+\left(\frac{\mathrm{d}z}{\mathrm{d}\zeta}\right)^2\right]^{\frac{1}{2}}\mathrm{d}\zeta. \tag{39}$$

Other geometric quantities in the integral equations such as $G(\boldsymbol{p},\boldsymbol{q})$ and $\nabla G(\boldsymbol{p},\boldsymbol{q})$ are computed from the above equations. The most stable calculations were performed with the density functions ϕ and $\partial\phi/\partial n$ inside each panel interpolated as cubic spline and linear functions of s, respectively.

The spline fitting of the surface during penetration is complicated by the presence of the triple point where the common surface attaches to the ring bubble. In the present

work, the surface is fitted continuously from the north pole to south pole by a path covering S^+, S_b and S^- sequentially. As a result, the normal to the surface directed into the fluid changes continuously during the integration around the surface and a cusp is formed in the bubble at the triple point (see figure 1*b*). This treatment is based on the fact that at the final stage of the bubble collapse, the speed of the surface of the re-entrant jet is generally on the order of 10^1–$10^2(\Delta P/\rho)^{\frac{1}{2}}$ while the fluid near the wall is moving more slowly in the opposite direction. Thus, there exists a strong shear layer in the region close to the triple point. In experiments, this shear layer contains a layer of gas. A similar flow is generated when a liquid jet impacts on a flat water surface and air entrainment occurs along the periphery of the jet. Surface tension forces have the tendency to round the cusp, but in the present case this does not occur owing to the effects of inertia and the short timescale.

Since the problem is axisymmetric about the z-axis, the terms in the integral equations can first be integrated analytically with respect to the circumferential variable θ. The resulting terms then involve elliptical integrals of the first and second kinds as functions of the arclength s in the $\theta = 0$ plane (see Appendix C). The field points (collocation points or nodes) are taken at the edge points of the panels. As a result, the integral equations (20) and (21) can be written in discretized forms within each panel,

$$\sum_{j=m}^{n_b-m+1} \int_{L_j} \left[C_{ij} \left(\frac{\partial \phi}{\partial n}\right)^j + D_{ij} \phi^j \right] \mathrm{d}s_j + \sum_{j=1}^{m-1} \int_{L_j} D_{ij} [(\phi^+)^j - (\phi^-)^j] \, \mathrm{d}s_j + J_1 = \begin{cases} 2\pi\phi_i; & i = m+1, \ldots, n_b-m+1 \\ 2\pi(\phi_i^+ + \phi_i^-); & i = 1, \ldots, m, \end{cases} \tag{40}$$

$$\sum_{j=m}^{n_b-m+1} \int_{L_j} \left[E_{ij} \left(\frac{\partial \phi}{\partial n}\right)^j + F_{ij} \left(\frac{\partial \phi}{\partial s}\right)^j \right] \mathrm{d}s_j + \sum_{j=1}^{m-1} \int_{L_j} F_{ij} \left[\left(\frac{\partial \phi}{\partial s^+}\right)^j + \left(\frac{\partial \phi}{\partial s^-}\right)^j \right] \mathrm{d}s_j + J_2 = \begin{cases} 2\pi(\partial\phi/\partial n)_i; & i = m+1, \ldots, n_b-m+1 \\ 4\pi(\partial\phi^+/\partial n)_i; & i = 1, \ldots, m, \end{cases} \tag{41}$$

where m is the index of the triple point; i and j represent the indexes of the field point and source panel, respectively; L_j is the arclength of panel j; J_1 and J_2 are the terms corresponding to the contribution from the image bubble; C_{ij}, D_{ij}, E_{ij} and F_{ij} are functions of the elliptic integrals and can be found in Appendix C; ϕ^j, $(\partial\phi/\partial n)^j$ and $(\partial\phi/\partial s)^j$ are functions of the arclength inside the panel j; and ϕ_i and $(\partial\phi/\partial n)_i$ are values at the point i. Gauss–Legendre quadrature formulae were used to calculate the integrals in (40) and (41), in which the regular integrands were integrated with a 5-point formula while the non-regular integrands, which contain logarithmic singularities, were treated with the formulation given by Anderson (1965). The linear system of algebraic equations formed in this way were solved with the LDU Algorithm (Press *et al.* 1989).

Various combinations of (40) and (41) were applied at the nodes during different phases of the calculations. For cases without a common surface, two combinations were used. In some cases the CBIE was applied at all the nodes. In other cases, the HBIE was applied at the first n_d nodes on top of the bubble starting with the north pole and the last n_d nodes ending with the south pole while the CBIE was applied at the remaining n_b+1-2n_d nodes. In cases during penetration with m double nodes along the common surface, the HBIE was applied at the first n_d+1-m nodes starting with the north pole and the CBIE was applied to the last m nodes ending with the south pole.

The adjustment of the time step during the impact of adjacent nodes was found to be critical to achieving an accurate calculation. The general technique employed here was to adjust the time step so that, given the distance and relative velocity between the nodes at the current time, the nodes would impact at the end of the time step. To implement this scheme a minimum distance ϵ was chosen. If the distance between one or more pairs of nodes on the ring bubble adjacent to the triple point was less than ϵ, the time step was adjusted so that all of these pairs collided by the end of the time step. In performing the calculations, it was found that as ϵ was decreased the calculation converged initially. However, if ϵ was too small, an overlapping of the nodes on the ring bubble near the triple point occurred at the next time step. It is thought that these problems arise because the Green's function between nearly touching nodes from opposite sides of the bubble becomes singular as the distance between the nodes tends to zero. Thus, for small enough ϵ the solutions of the boundary integral equations are probably inaccurate. After a number of test calculations, it was found that $\epsilon = 0.002$ was a typical minimum value that produced a converged calculation without overlapping of adjacent nodes. This value was used for all the calculations presented in this paper.

3.5. *Numerical instabilities*

The numerical method presented above exhibits unstable behaviour when the volume of the ring bubble approaches the initial volume of the bubble. The causes of the numerical instability are not clear. There is no theoretical analysis available to examine the numerical instability because the boundary conditions (4), (10) and (13) are coupled and the conditions (10) and (13) are nonlinear. Several researchers (Longuet-Higgins & Cokelet 1976; Dommermuth & Yue 1987; Oğuz & Prosperetti 1990) have reported similar instabilities encountered in boundary element calculations employing higher-order elements when simulating nonlinear waves and water droplets.

To cope with the instabilities, a 5-point smoothing technique (Mathematical Handbook 1977, pp. 907–908) was introduced. Given a data set $y_i (i = 0, 1, 2, \ldots, m)$, the modified data set $y_i' (i = 0, 1, 2, \ldots, m)$ is computed by the following smoothing formulations:

$$y_i' = \tfrac{1}{35}[-3(y_{i-2}+y_{i+2})+12(y_{i-1}+y_{i+1})+17y_i], \quad i = 2, \ldots, m-2, \tag{42}$$

$$y_0' = \tfrac{1}{35}(31y_0+9y_1-3y_2-5y_3+3y_4), \tag{43}$$

$$y_1' = \tfrac{1}{35}(9y_0+13y_1+12y_2+6y_3-5y_4), \tag{44}$$

$$y_{m-1}' = \tfrac{1}{35}(-5y_{m-4}+6y_{m-3}+12y_{m-2}+13y_{m-1}+9y_m), \tag{45}$$

$$y_m' = \tfrac{1}{35}(3y_{m-4}-5y_{m-3}-3y_{m-2}+9y_{m-1}+31y_m). \tag{46}$$

Mesh regridding is also adopted to keep equal panel sizes during the time stepping.

4. Verification of the numerical modelling

In this section, the results of several static and dynamic tests designed to verify the mathematical model and to assess the performance of the combined numerical scheme developed in §§2 and 3 are presented.

4.1. *A sheet attached to a toroid*

The first test of the numerical model is to examine the accuracy of the boundary element solver with the combined scheme on a static problem. In order for this test to have relevance to the penetration problem, it must satisfy the following conditions: the boundary geometry must include both regular and common surfaces, across the

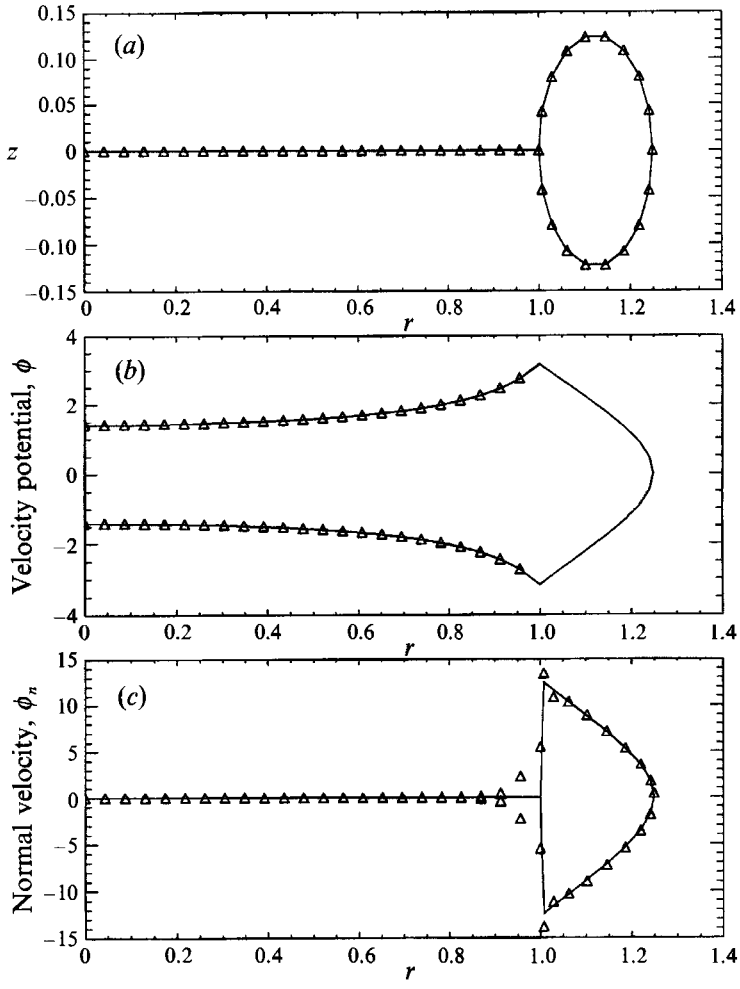

FIGURE 2. Comparisons of the results of the combined scheme with analytical solutions for a toroidal surface and a two-layer sheet. (*a*) Geometry of the sheet, toroid and mesh distributions (△, nodal point). (*b*) Calculated (△) and analytical (——) ϕ on the sheet. (*c*) Calculated (△) and analytical (——) $\partial\phi/\partial n$ on the sheet and toroid.

common surface ϕ and $\partial\phi/\partial s$ must be discontinuous while $\partial\phi/\partial n$ must be continuous, $|\nabla\phi|$ must vanish at infinity, and ϕ must be sufficiently continuous inside the domain. The boundary geometry of the chosen problem is that of a toroid about the z-axis connected to a flat circular sheet on the plane $z = 0$ as shown in figure 2(*a*). In the domain exterior to this boundary, Laplace's equation can be easily solved in toroidal coordinates (η, θ, ψ) given by the following transformations (for axisymmetric problems):

$$x = \frac{a\sinh(\eta)}{\cosh(\eta)-\cos(\theta)}, \tag{47}$$

$$z = \frac{a\sin(\theta)}{\cosh(\eta)-\cos(\theta)}. \tag{48}$$

Thus, the cross-section of the toroid is given by $\eta = \eta_0$, $-\pi \leqslant \theta \leqslant \pi$ and $\psi = 0$ in the (η, θ, ψ) system or $(x - a\coth\eta_0)^2 + z^2 = a^2/\sinh^2(\eta_0)$ and $y = 0$ in the (x, y, z) system,

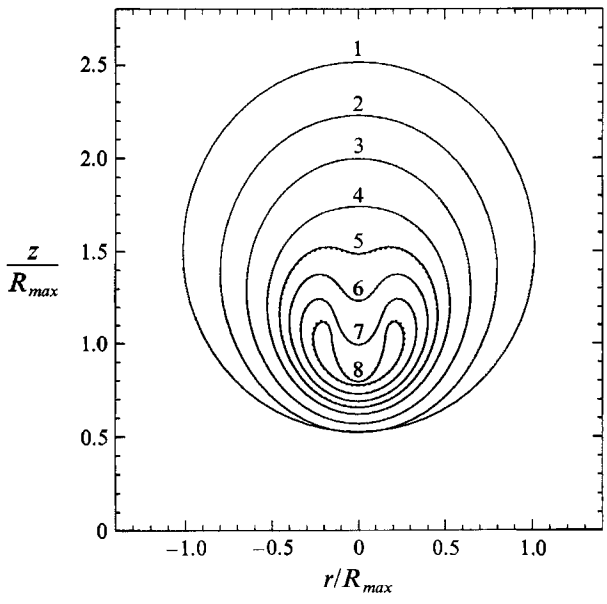

FIGURE 3. Comparison of bubble profiles between the conventional (——) and combined (·····) schemes for a transient cavitation bubble collapsing near a rigid wall with $R_0 = 0.1$ and $Z_0 = 1.5$. The numbers 1 to 8 correspond to the non-dimensional times $t = 0.983$, 1.707, 1.877, 1.972, 2.014, 2.043, 2.068, and 2.086.

while the cross-section of the sheet is given by $0 \leqslant \eta \leqslant \eta_0$, $\theta = \pm\pi$ and $\psi = 0$ or $0 \leqslant x \leqslant a\coth\eta_0 - a/\sinh\eta_0, y = 0$ and $z = 0$ in the two different coordinate systems, respectively. In the present test, η_0 is chosen as 2.890454 and a is 1.117637. From the infinite number of particular solutions of Laplace's equation in the (η, θ, ψ) system (Moon & Spencer 1961, pp. 369–372), one is chosen such that it satisfies the requirements of the numerical tests cited above. Thus, given ϕ on the sheet and the toroid in the form

$$\phi(\eta, \theta) = (\cosh(\eta) - \cos(\theta))^{\frac{1}{2}} \sin(\tfrac{1}{2}\theta), \tag{49}$$

the corresponding expressions for $\partial\phi/\partial n$ are, respectively,

$$\partial\phi/\partial n = 0 \quad \text{on the sheet,} \tag{50}$$

$$\partial\phi/\partial n = (\cosh(\eta) - \cos(\theta))^{\frac{1}{2}} \sinh(\eta) \sin(\tfrac{1}{2}\theta)/(2a) \quad \text{on the toroid.} \tag{51}$$

In the numerical calculations, ϕ was specified on the toroid and $\phi^+ - \phi^-$ was specified on the sheet from the analytical solution (49). The integral equations (20) and (21) were then solved with the combined scheme for $\partial\phi/\partial n$ on the entire surface and ϕ on the sheet. The comparison between the analytical and numerical calculations of ϕ on the sheet and $\partial\phi/\partial n$ on both the sheet and toroid are plotted in figures 2(*b*) and 2(*c*). The results show that the numerical calculations agree well with the analytical ones with the errors in $\partial\phi/\partial n$ and ϕ at the north pole less than 0.3% and 0.2%, respectively. The deviation of $\partial\phi/\partial n$ near the triple point between the sheet and toroid is as expected because the numerical scheme is constructed on the basis of a smooth surface generated by a cubic-spline fitting rather than a non-smooth connection at that point as in this test case. This is not considered to be a problem since, in the simulation of the penetration process, the tangent along the bubble surface is always assumed to vary continuously.

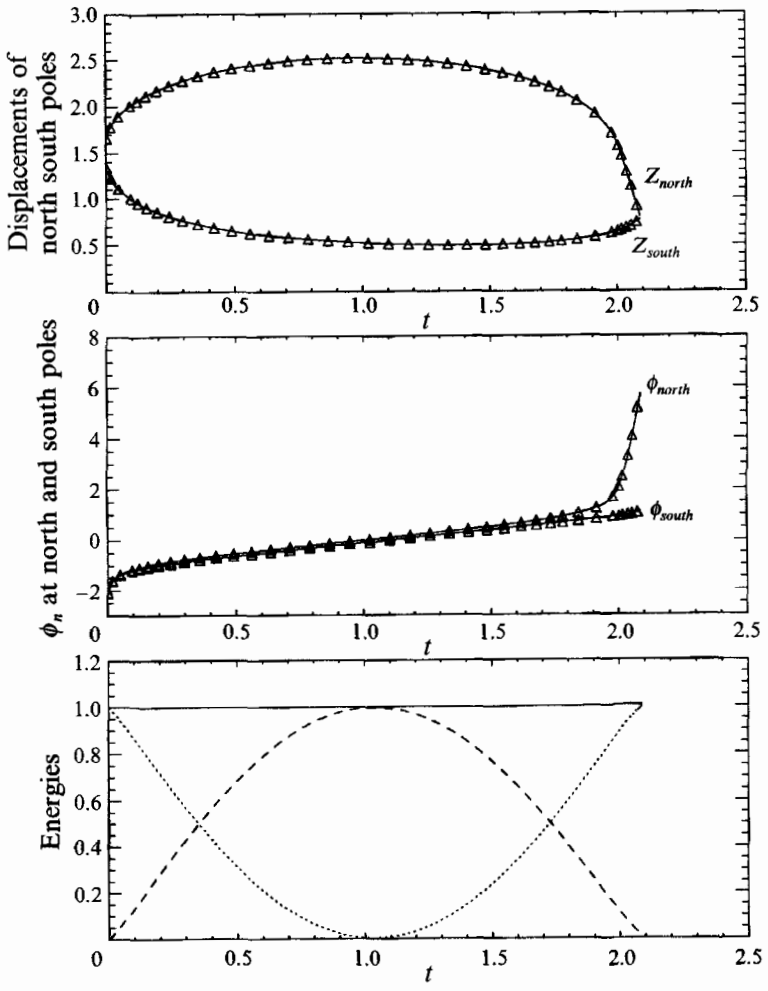

FIGURE 4. Various quantities plotted versus time for the bubble collapse depicted in figure 3. (*a*) The *z*-coordinates of the north and south poles of the bubble: ——, conventional scheme; △, combined scheme. (*b*) The velocity potentials at the north and south poles versus time: ——, conventional scheme; △, combined scheme. (*c*) The energies versus time for the combined scheme: total mechanical energy (——), kinetic energy (·····), and potential energy (– – –).

4.2. *A cavitation bubble collapsing near a rigid wall*

As a dynamic test, the combined scheme was used to compute the growth and collapse of a cavitation bubble adjacent to a rigid wall up to the time just before penetration begins. Because there is no analytical solution available for this non-spherical collapse case, the numerical calculations using the combined scheme are compared with those using the CBIE scheme. The results of the present CBIE scheme were compared to similar calculations in the literature and found to be in excellent agreement. Initially, the bubble is spherical and centred at $r = 0$ and $Z_0 = 1.5$ with radius $R_0 = 0.1$. The combined scheme was used with $n_b = 32$ and $n_d = 16$. Linear isoparametric elements were employed for the conventional scheme, also with $n_b = 32$. In figure 3, the bubble profiles at different time instants in the collapse phase obtained by both the combined and conventional scheme are plotted together. Both schemes give almost the same

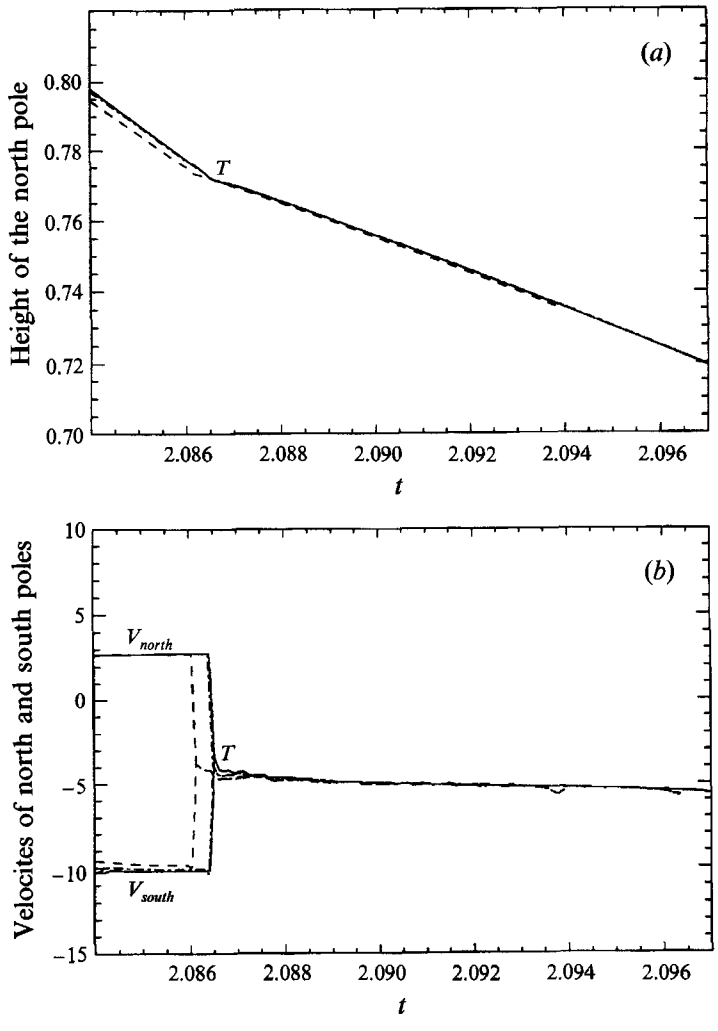

FIGURE 5. Convergence as a function of mesh size for the combined scheme before and after penetration. (*a*) The height of the north pole versus time; (*b*) the normal velocity of the north and south poles versus time. ——, $n_b = 32$; –·–·–, $n_b = 48$, and ——, $n_b = 64$. T denotes the instant of initial impact.

bubble profiles at the same time. The heights of the north and south poles, the velocity potentials at the north and south poles and the kinetic and potential energies of the flow are plotted versus time in figures 4(*a*), 4(*b*) and 4(*c*), respectively, for both schemes. There is good agreement in all cases.

4.3. *Convergence studies*

Several computations aimed at examining the convergence of the combined scheme versus panel size and time step size during penetration simulations were also made. Figure 5(*a*) and 5(*b*) show the height and velocity of the north pole from before penetration through the penetration process for various panel numbers. As can be seen from the figure, the results converge as the number of panels increases. Figures 6(*a*) and 6(*b*) show the same quantities converging as the time step decreases. The number of panels and time step used in the present results are given in the following section.

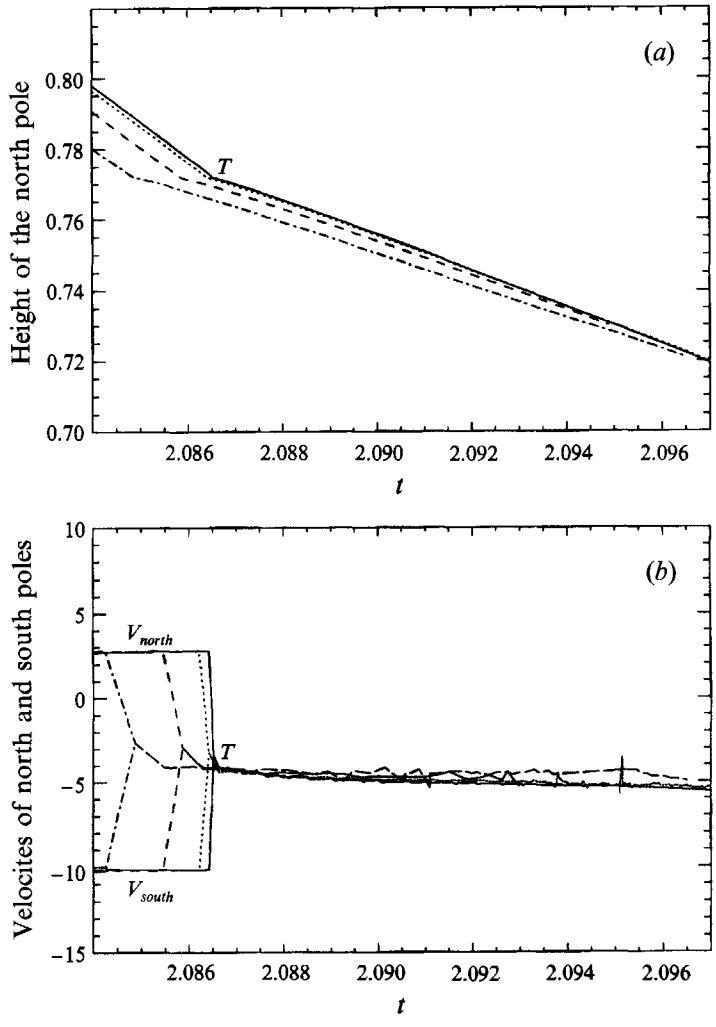

FIGURE 6. Convergence as a function of time step size for the combined scheme before and after penetration. (*a*) The height of the north pole versus time; (*b*) the normal velocity of the north and south poles versus time. –·–·–, $C = 0.06$; – – –, $C = 0.04$; ·····, $C = 0.02$; ——, $C = 0.01$. The parameter C is related to the variable time step, $\Delta t = C/(1+0.5V_{max}^2)$. T denotes the instant of initial impact.

The tests conducted in this section show that the combined scheme developed in §§2 and 3 is valid in both static and dynamic cases.

5. Simulation of the penetration process

The calculations presented in this section were done with $n_b = 64$ and $R_0 = 0.1$. From the initial instant up to the time when the distance between the north and south poles becomes less than 0.03, the CBIE method is used for all nodes. At this point, the scheme is switched to the combined CBIE–HBIE method with $n_d = 32$. When penetration begins, the scheme is again switched to that described in §3.4 for cases with a common surface. The parameter C for time stepping is taken as 0.04 before penetration and 0.01 during penetration. The value of ϵ is chosen as 0.002 (see §3.4).

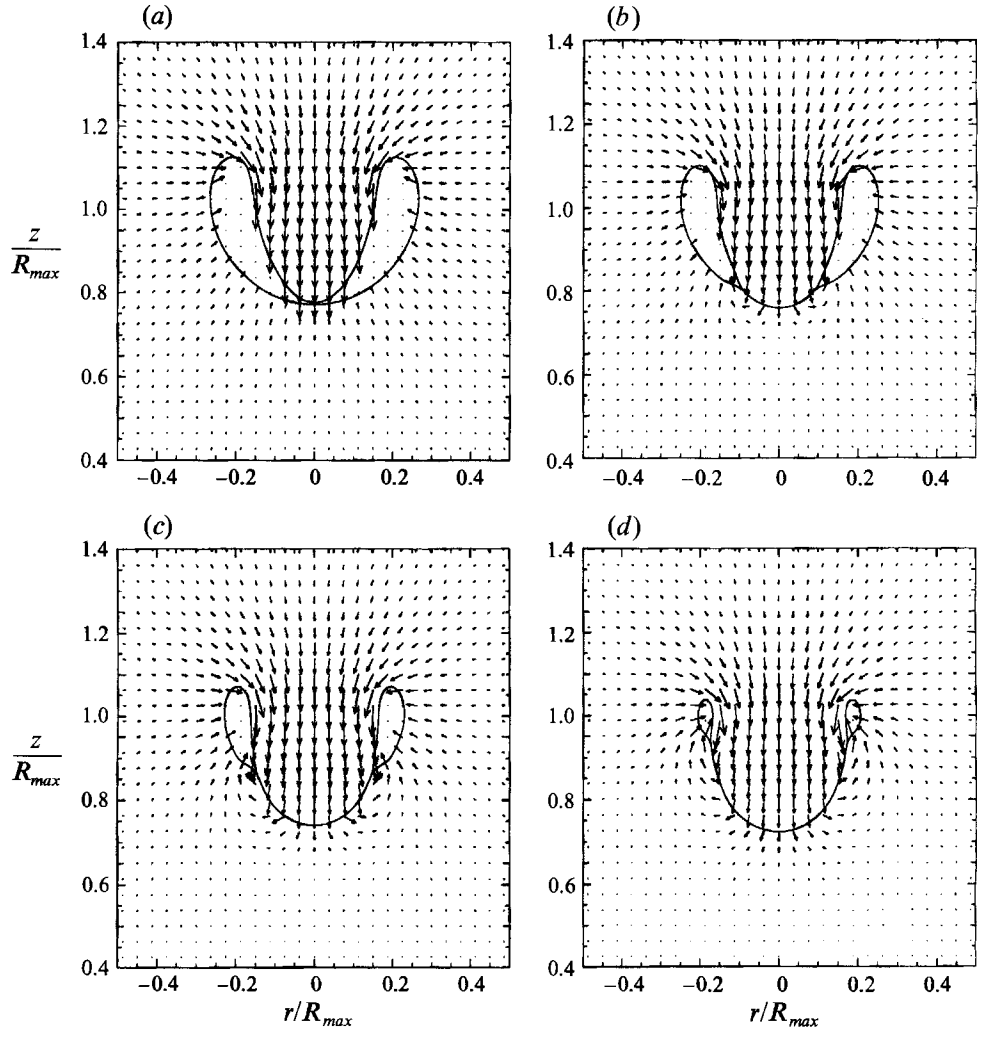

FIGURE 7. Bubble profiles and velocity fields for $Z_0 = 1.5$ and $R_0 = 0.1$: (*a*) $t = 2.08545$, (*b*) $t = 2.08861$, (*c*) $t = 2.09241$, (*d*) $t = 2.09551$. The lengths of the velocity vectors are scaled with respect to the flow speeds at the location ($r = 0$, $z = 1.1375$) in each plot. These speeds are 8.43, 7.94, 7.17 and 6.30 in (*a*), (*b*), (*c*) and (*d*), respectively.

Z_0	T_c	Z_c	V_n	V_s	V_c	Γ_{ns}
1.1	2.16048	0.099	−9.055	0.042	−4.254	5.400
1.25	2.13679	0.318	−8.459	1.126	−4.167	5.331
1.5	2.09013	0.777	−11.574	3.480	−4.079	4.717
1.75	2.05396	1.172	−12.013	4.550	−4.235	4.371

TABLE 1. Z_0: initial height of the bubble centroid; T_c: collpse time; Z_c: collapse height (z of north and south pole at $t = T_c$); V_n: velocity of the north pole before impact (in the $-z$ direction); V_s: velocity of the south pole before impact; V_c: velocity of the north (or south) pole just after the initial impact; Γ_{ns}: circulation around the ring bubble at the instant of the initial impact

In the following, results are presented for $Z_0 = 1.1$, 1.25, 1.5 and 1.75. The results for $Z_0 = 1.5$ and 1.1 are presented first and in more detail than those for the other Z_0 values. For reference throughout the discussion, table 1 gives the time (T_c), the height (Z_c), the velocities of the north and south poles of the bubble (V_n and V_s) at the instant before initial impact and the velocity of the north pole of the sheet (V_c) as well as the circulation (Γ_{ns}, defined below) at the instant after initial impact for all four values of Z_0.

5.1. *Bubble profiles and velocity fields*

The general features of the flow field just before and during penetration are illustrated in figure 7, for $Z_0 = 1.5$. Figure 7(*a*) shows the flow field one time step before penetration. The re-entrant jet has formed at the top of the bubble surface and is moving toward the rigid wall. The fluid on the lower side of the bubble has not yet sensed the jet and is still moving away from the wall. The relative normal velocity between the north and south poles at this instant is 15.05 (see table 1). The poles of the bubble meet at $z = 0.78$ and the flow field soon after penetration is shown in figure 7(*b*). As can be seen in the figure, the geometry of the bubble surface has become a ring bubble with an attached sheet. The flow pattern has suddenly changed such that the flow on the lower side of the bubble has reversed direction and is now moving toward the wall. The velocity of the re-entrant jet is still directed toward the wall but with a much smaller magnitude (4.08) than before impact (11.57). The velocity components tangent to the common surface and the ring bubble surface are directed mainly toward the axis of symmetry on the jet side of the common surface and bubble and away from the axis on the other side; this indicates that there are vortex elements along the sheet and in the bubble that circle the z-axis. The mechanism that brings about this sudden change in the flow field is the liquid–liquid impact during jet penetration.

Further development of the penetration process is shown in figure 7(*c*). The dominant changes in the bubble profile are the drastic reduction in the volume of the ring bubble and the extension of the vortex sheet due to continuing impacts of the surface panels of the ring bubble. There is also some translational motion of the bubble and the sheet in the direction of the rigid wall. In figure 7(*d*), the volume of the ring bubble has reached about 0.72 times the initial bubble volume. The calculation becomes unstable soon after this time. It is presumed that if gas were included in the bubble, the bubble would begin a second growth phase at approximately this time, depending on the amount of gas. The flow pattern in figure 7(*d*) is characterized by a large vortex sheet attached to a small ring bubble with a rotating flow concentrated in the area around the ring bubble in the vicinity of the triple point.

Bubble profiles and velocity fields for $Z_0 = 1.1$ are given in figure 8. As in the previous case, the impact of the re-entrant jet results in the formation of a ring bubble and a vortex sheet. At the instant before initial impact, the north and south poles of the bubble are much closer to the wall ($z = 0.10$) than in the previous case and the relative normal velocity between the north and south poles is 9.10 compared to 15.05 for $Z_0 = 1.5$, see table 1. The remaining bubble volume at the instant of impact (46.19 for $Z_0 = 1.1$) is much larger than in the case for $Z_0 = 1.5$. Later in the penetration process, the tip of the vortex sheet hits the rigid wall for $Z_0 = 1.1$ (figure 8*c*, *d*) while the tip of the sheet for $Z_0 = 1.5$ is still relatively far away from the wall even at the end of the first collpse. The shape of the vortex sheet also shows marked differences between the two cases. For $Z_0 = 1.5$, the vortex sheet is 'U'-shaped while for $Z_0 = 1.1$ the sheet rolls up at the sides due to the stronger influence of the wall. The calculation for $Z_0 = 1.1$ is terminated when the bubble volume is reduced to about 7.1 times its initial volume because of numerical instabilities.

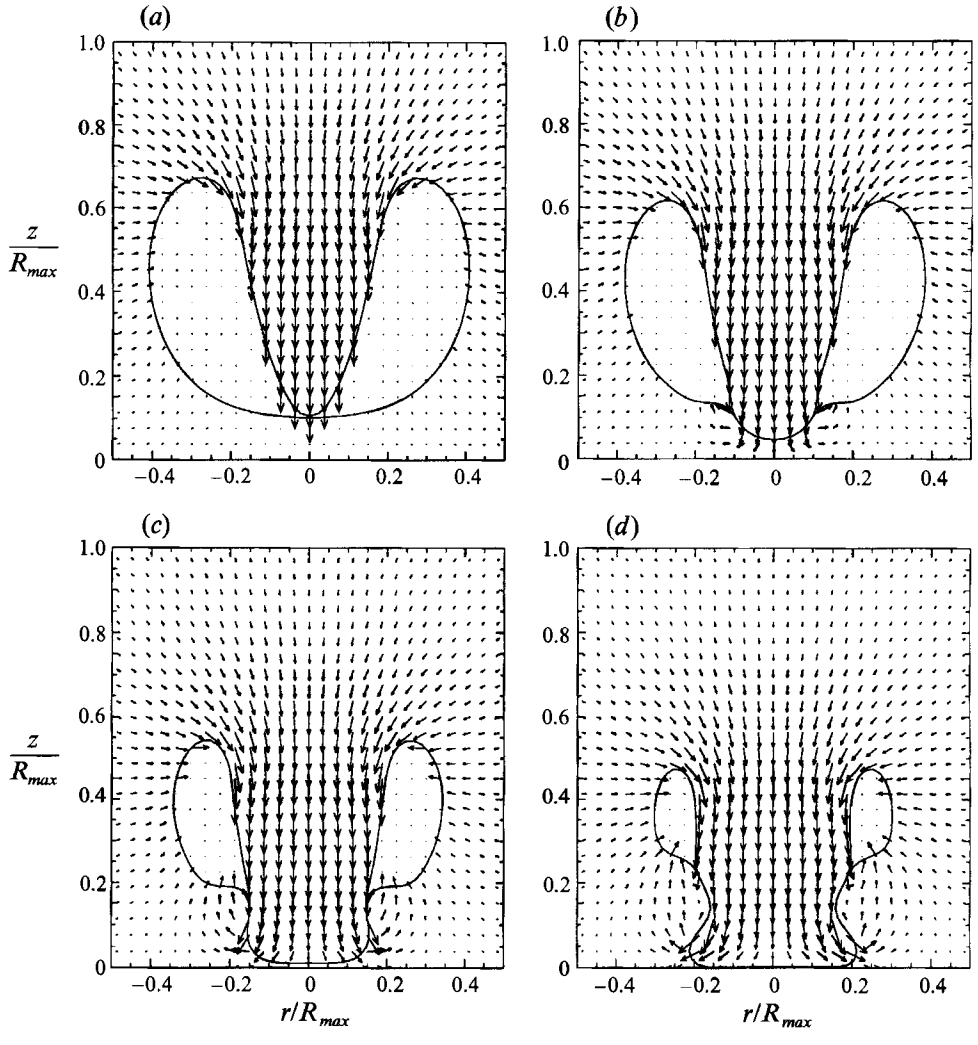

FIGURE 8. Bubble profiles and velocity fields for $Z_0 = 1.1$ and $R_0 = 0.1$: (*a*) $t = 2.15059$, (*b*) $t = 2.16400$, (*c*) $t = 2.18074$, (*d*) $t = 2.19429$. The lengths of the velocity vectors are scaled with respect to the flow speeds at the location ($r = 0$, $z = 0.7125$) in each plot. These speeds are 5.16, 4.30, 3.24 and 2.45 in (*a*), (*b*), (*c*) and (*d*), respectively.

5.2. *Pressure fields*

The pressure at any point in the fluid domain was computed from the non-dimensional Bernoulli equation,

$$\frac{P-P_\infty}{P_\infty-P_0} = -\frac{\partial\phi}{\partial t} - \frac{1}{2}\left[\left(\frac{\partial\phi}{\partial r}\right)^2 + \left(\frac{\partial\phi}{\partial z}\right)^2\right]. \tag{52}$$

The required spatial and temporal derivatives of ϕ were calculated by finite difference from local values of ϕ that are calculated from the integral equations (A 7) and (A 13) in Appendix A using values of ϕ and $\partial\phi/\partial n$ on the surface of the bubble and the vortex sheet. Note that the pressure can be computed after the calculation of the bubble motion is completed. Unfortunately, during penetration, at each time instant when new surface panels of finite size come together, ϕ goes through finite jumps as can be

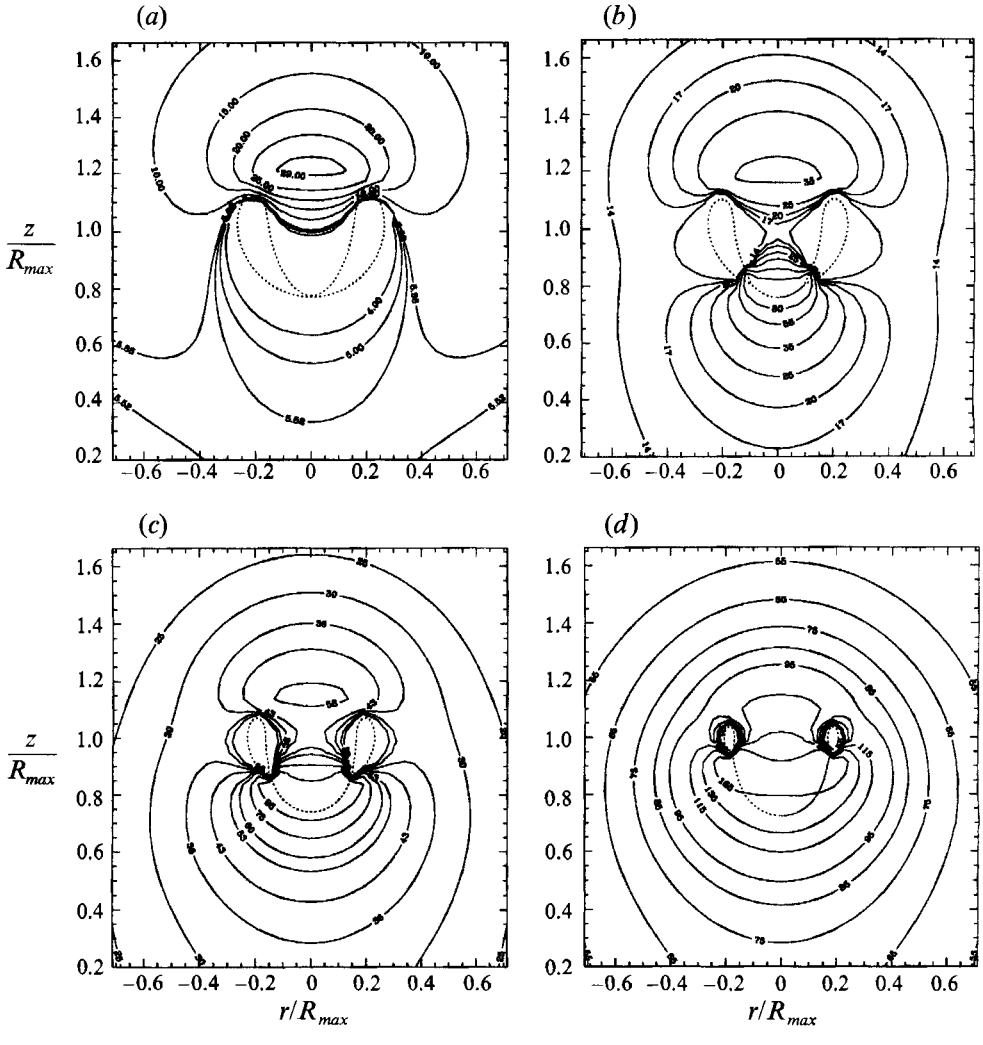

FIGURE 9. Pressure contours for $Z_0 = 1.5$ and $R_0 = 0.1$: (*a*) $t = 2.08545$, (*b*) $t = 2.08861$, (*c*) $t = 2.09241$ and (*d*) $t = 2.09551$. The bubble profiles are shown as a dotted line.

seen from (15). These jumps cause the derivative of ϕ with respect to time, and thus the pressure, to fluctuate wildly. If the panel size were infinitesimal these jumps in ϕ would also be infinitesimal and the pressure would vary rapidly but in a smooth manner. To remedy this problem, a linear least-squares fitting technique was used to smooth ϕ in a given time interval before computing $\partial\phi/\partial t$ and the pressures.

Corresponding to the flow fields in figure 7(*a–d*) for $Z_0 = 1.5$, four plots of the pressure contours are presented in figure 9(*a–d*), respectively. The pressure contours are given as solid lines while the profiles of the bubble are shown as dotted lines. The pressure field one step before penetration is given in figure 9(*a*). The highest pressure region in the field is within the contour with magnitude 29 which is located on the *z*-axis above the bubble. The pressure field just after impact, figure 9(*b*), is dramatically different than that before impact. The highest pressure region in figure 9(*b*) is at the tip of the jet where the magnitude of the enclosing contour is 80. This high-pressure buildup at the penetration interface in turn causes a large deceleration of the fluid in

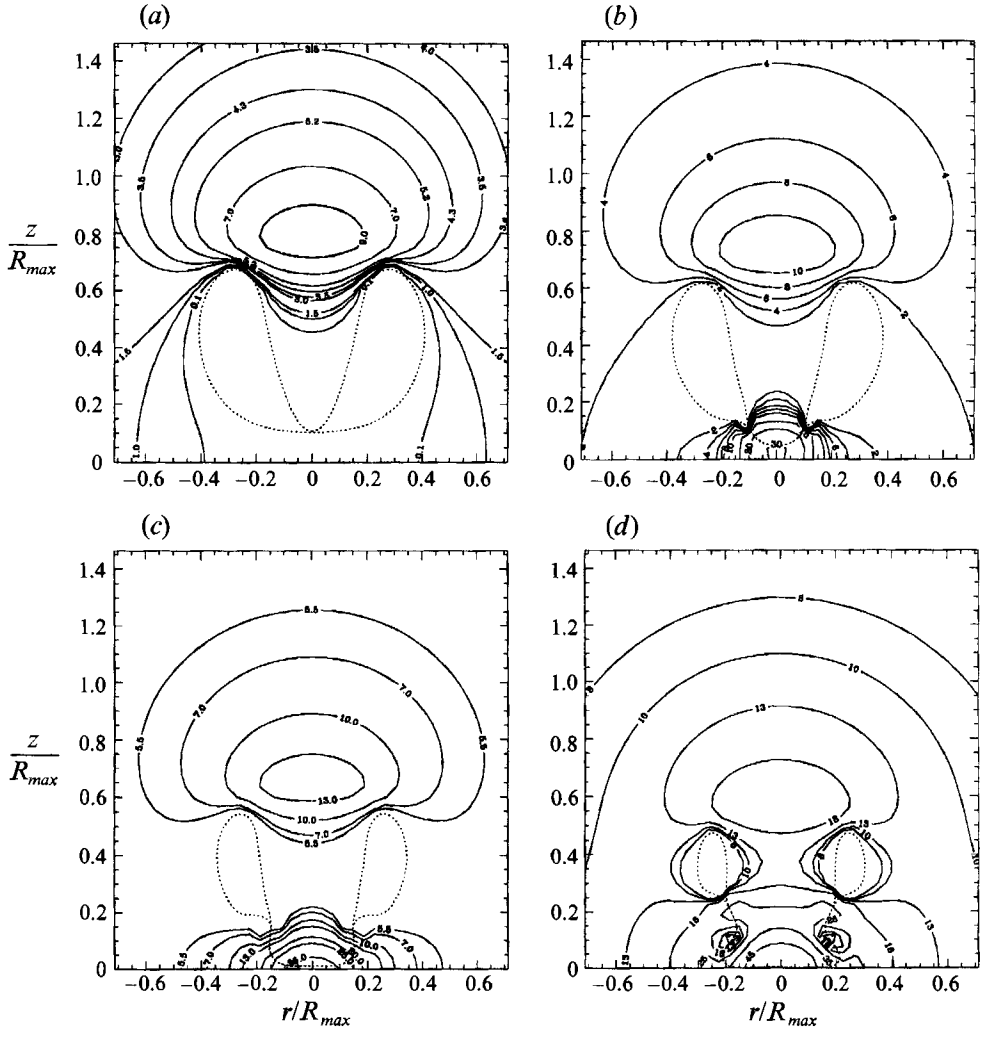

FIGURE 10. Pressure contours for $Z_0 = 1.1$ and $R_0 = 0.1$. (*a*) $t = 2.15059$ and (*b*) $t = 2.16400$, (*c*) $t = 2.18074$ and (*d*) $t = 2.19429$. The bubble profiles are shown as dotted lines.

the re-entrant jet and an acceleration toward the wall of the fluid between the sheet and the wall. From the pressure contours in figure 9(*c*, *d*), it can be seen that the pressure at the penetration interface continues to increase, reaching 165 in the final figure. The pressure contours far from the bubble are nearly circular at this time.

The pressure contours corresponding to the velocity fields in figure 8(*a*–*d*) for $Z_0 = 1.1$ are presented in figure 10(*a*–*d*), respectively. As can be seen from figure 10(*a*), at the instant just before penetration, a high-pressure region is again located on the *z*-axis above the bubble. The maximum pressure contour in this case is 9, considerably less than in the case for $Z_0 = 1.5$. Immediately following the initial impact, figure 10(*b*), large pressures are located around the impact interface. The pressure contour surrounding this region has a magnitude of 30 and intersects the wall. The further development of the pressure fields is given in figure 10(*c*, *d*) from which it can be seen that the pressure reaches more than 45 at the penetration interface and the wall. It should be noted that the high-pressure region on the wall covers a smaller area for

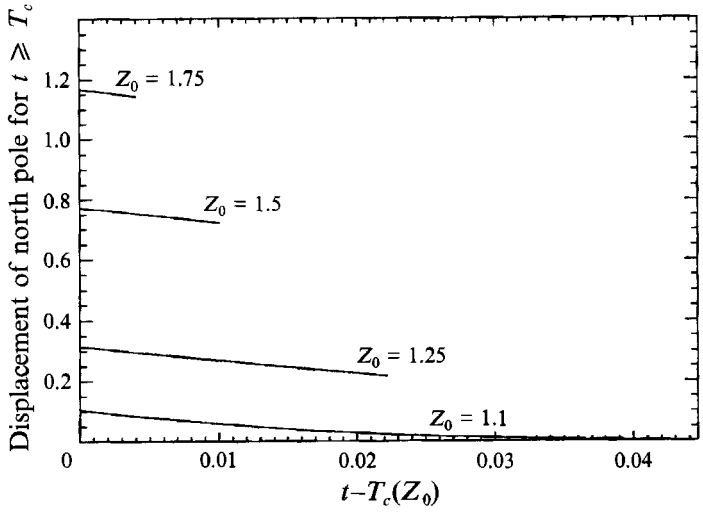

FIGURE 11. The displacements of the north pole on the common surface for various values of Z_0 as functions of time after initial impact, $t - T_c(Z_0)$.

$Z_0 = 1.1$ compared to $Z_0 = 1.5$. This concentration may be partially responsible for the well-known increase in the potential for surface damage as Z_0 is decreased. Also of interest in figure 10(*d*) are the two pairs of closed low-pressure contours. The upper pair encloses the ring bubble while the lower pair, which is located near the bend in the vortex sheet, indicates the presence of a localized vortex-ring-like structure. This structure is also visible in the velocity contours in figure 8(*d*).

5.3. *Motion of the north and south poles*

In this and the following subsections, selected quantities from four calculations with $Z_0 = 1.75$, 1.5, 1.25 and 1.1 are examined as functions of time. In order to make comparisons of various quantities after initial impact, it was decided to define a common time origin, T_c, the time when the north and south poles of the bubble meet at the instant of initial impact. From the data in table 1, it can be seen that T_c increases with decreasing Z_0. The heights of the north pole for the four cases are plotted in figure 11. After initial impact, the north pole is defined as the point where the vortex sheet intersects the z-axis. As can be seen from figure 11, the north pole continues moving toward the wall after the initial impact in all cases. The relative velocity of the north and south poles of the bubble just before initial impact can be found in table 1 along with the velocity of the vortex sheet just after initial impact. The relative velocity, $V_s - V_n$, decreases steadily from 16.56 at $Z_0 = 1.75$ to 9.10 at $Z_0 = 1.1$; however, the speed of the jet tip just after initial impact is between 4.1 and 4.25 in all four cases. The slope of the curves in figure 11 indicates the velocities of the north poles. As can be seen from the figure the velocity is relatively constant after initial impact for the larger Z_0; however, for small Z_0, the velocity decreases with time and is nearly zero at the end of the collapse for $Z_0 = 1.1$.

5.4. *Pressure at the centre of the wall*

In figures 12(*a*) and 12(*b*), the velocity potential ϕ and the pressure on the wall directly under the centre of the bubble ($(r, z) = (0, 0)$) are plotted versus time for different Z_0. Note that the plot of ϕ starts at $t = 0$ while the plot of the pressure starts fairly late in

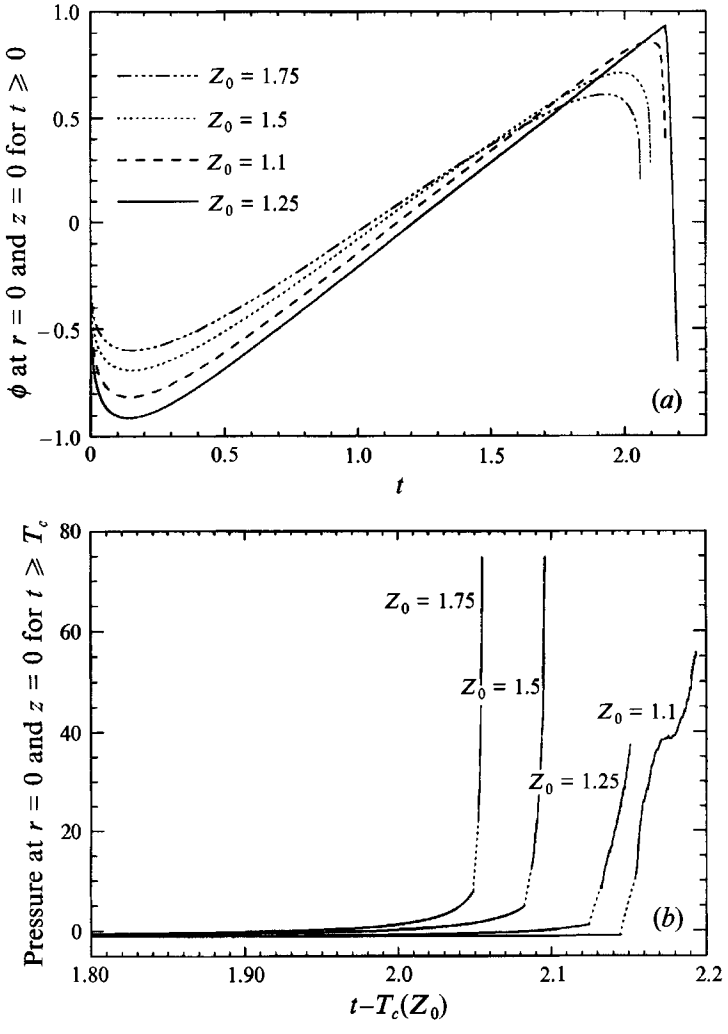

FIGURE 12. (*a*) The velocity potential and (*b*) the pressure at the centre of the rigid wall for various values of Z_0 as functions of time.

the collapse phase, $t = 1.80$. From Bernoulli's equation (52), the pressure at the centre of the wall is equal to $-\partial\phi/\partial t$ since $\boldsymbol{u} = 0$ at this location. Thus, the pressures plotted in figure 12(*b*) were obtained by differentiating the curves of ϕ in figure 12(*a*). Before differentiation, the ϕ-data were smoothed with a running 40-point least-squares fit of a second-order polynomial in order to eliminate the jumps in ϕ caused by the panel impacts. Each pressure curve has a short gap near the time of the initial impact. This gap is due to the inability of the second-order polynomial to fit the ϕ-data well due to the rapid fluctuations at that point in time. All cases show sudden rises in the pressure during jet penetration. For the case of $Z_0 = 1.1$, there is a plateau in the pressure after initial impact at about the time when the vortex sheet reaches the wall.

Figure 12(*b*) provides useful information of the time history of the pressure at the centre of the wall. However, it should be pointed out that the 'maximum' values in this plot occur while the pressure is still rising at the point when the calculations terminate due to numerical instabilities. To obtain a true maximum value of the impulsive

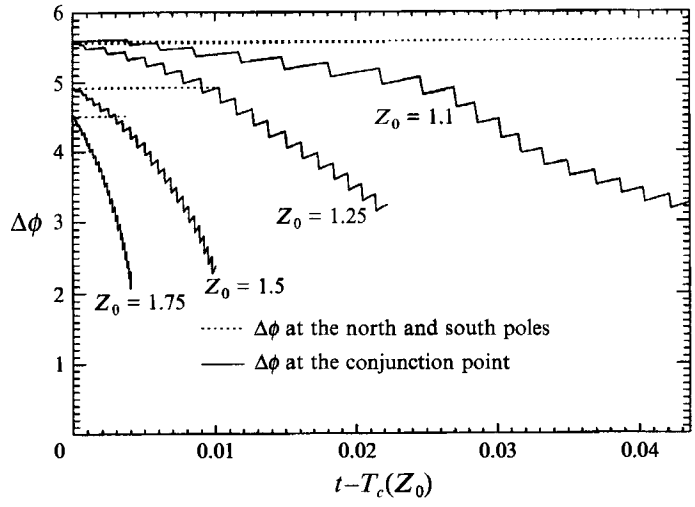

FIGURE 13. The total circulation, $\Gamma_{ns} = \phi^+_{np} - \phi^-_{sp}$, and the circulation associated with the ring bubble, $\phi^+_T - \phi^-_T$, versus time after initial impact, $t - T_c(Z_0)$, for various values of Z_0.

pressure on the wall, a rebounding mechanism such as that provided by a non-condensible gas inside the bubble must be considered. A study of the impulsive pressure due to a gas bubble collapse and rebound is currently underway.

5.5. *Circulation*

Before penetration, the fluid domain is simply connected and the bubble boundary is a regular surface. In this case, there is no circulation along any closed path inside the fluid. However, after initial impact, if a closed path is drawn such that it pierces the vortex surface, the circulation along this path is not zero, and the fluid domain is no longer simply connected. The generation of this circulation is due to the liquid–liquid impact rather than viscous effects. If a closed path is drawn starting from the south pole and ending at the north pole of the bubble and enclosing the sheet and ring bubble, the circulation for this path, Γ_{ns}, is given by $(\phi^+ - \phi^-)$ evaluated at $r = 0$. From (13) it is easy to show that

$$\frac{\mathrm{d}\Gamma_{ns}}{\mathrm{d}t} = \left.\frac{\mathrm{D}(\phi^+ - \phi^-)}{\mathrm{D}t}\right|_{r=0} = 0 \tag{53}$$

since $\partial\phi/\partial s = 0$ at $r = 0$. This finding was used in the two-step method of Best (1991) to choose a value of the circulation for the ring bubble. The values of Γ_{ns} are given in table 1. As can be seen from the table the circulation increases monotonically from 4.37 to 5.40 as Z_0 decreases from 1.75 to 1.1. It is also interesting to examine the division of the source of the circulation between the vortex sheet and the ring bubble. This division can be seen by comparing the total circulation, Γ_{ns}, to the circulation around the ring bubble, Γ_b, which is obtained with a path that starts at the triple point on the underside of the bubble, extends around the outer side of the bubble and ends on the top side of the bubble at the triple point. Thus, $\Gamma_b = \phi^+_T - \phi^-_T$, where the subscript T refers to the triple point. The values of the two circulations are plotted versus time in figure 13 for the four values of Z_0. The solid lines in this figure represent the circulations associated with the ring bubbles, Γ_b, while the differences between the dotted and solid lines are the circulations associated with the vortex sheets for different Z_0. As noted in the previous subsections, the step-like appearance of the plots is due

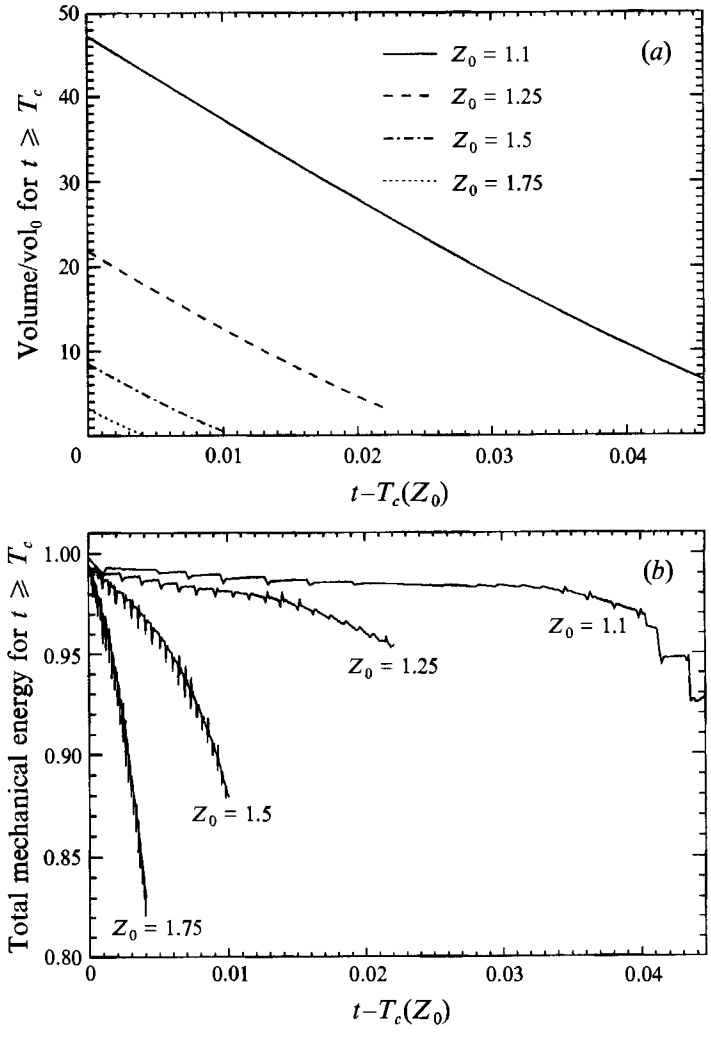

FIGURE 14. (*a*) The bubble volume, (Volume/Vol$_0$), and (*b*) the total mechanical energy for various values of Z_0 as functions of time after initial impact, $t-T_c(Z_0)$. Vol$_0$ is the initial bubble volume.

to the discrete panel impacts. This figure shows that, for all four cases, after penetration the circulation associated with the ring bubble decreases with time and, since the total circulation is constant, the circulation associated with the sheet increases with time. As Z_0 decreases, the rate of increase of circulation associated with the vortex sheet increases. At the end of the simulations the percentage of the total circulation associated with the sheet is on the order of 50% for the cases with larger Z_0.

5.6. *Energy*

The potential and kinetic energies of the flow were calculated using (22) and (23). Figure 4(*c*) is a plot of the potential, kinetic and total energy versus time from $t = 0$ up to the instant before initial impact for $Z_0 = 1.5$. As can be seen from the figure, the total energy is constant. Figures 14(*a*) and 14(*b*) give information on the energy versus time after initial impact. The potential energy is proportional to the bubble volume, which is plotted in figure 14(*a*). As can be seen from the figure, the volume at the first

instant of impact increases with decreasing Z_0. For example, the bubble volume for $Z_0 = 1.75$ has reduced to almost its initial volume at $t = T_c$ while the corresponding volume for $Z_0 = 1.1$ is about 48 times as large as its initial value. Note also from figure 14(*a*) that the bubbles with larger volume at the first instant of impact take a longer time to reach minimum volume while the rate of decrease in volume with time does not vary appreciably with Z_0. The total mechanical energy versus time after initial impact is presented in figure 14(*b*). As was noted in §2.5, the total mechanical energy of the system should decrease with time for $t > T_c$ owing to the liquid–liquid impacts of the panels. Energy loss should only occur at the time steps where an impact between two or more surface panels occurs. This behaviour is generally evident in the results of the calculation as is shown in figure 14(*b*) at early times for $Z_0 = 1.25$ and 1.1. It is believed that the changes in energy between impacts in the other calculations are caused by the extensive regridding of the surfaces necessitated by the movement of the panels from S_b to $S^+ \cup S^-$ combined with finite panel sizes and time steps. In general, the rate of energy loss with time increases as Z_0 is increased. For $Z_0 = 1.75$, the flow loses about 18% of its total energy by the time the calculation becomes unstable. When the calculation for $Z_0 = 1.1$ becomes unstable, the energy loss has reached only 7% of its original value. In a compressible flow this energy would primarily be radiated away in the form of sound or shock waves. In the present incompressible calculations this energy is effectively radiated away at infinite speed.

6. Conclusions

The final stage of the collapse of a cavitation bubble near a rigid wall has been simulated with a boundary element method. The method allows for the simulation of the growth and collapse of the bubble including the re-entrant jet impact and penetration processes that occur toward the end of the collapse. During the impact process, the bubble is transformed into a toroidal-shaped cavity (ring bubble). This ring bubble is attached to an impact interface that separates the fluid masses that were initially on opposite sides of the bubble. The impact interface is assumed to be infinitesimally thin and the pressure and the normal velocity across the interface are assumed to be continuous. This modelling allows for the formation of a vortex sheet along the interface.

The results of the calculation show that the impact of the re-entrant jet starts at a single point on the north and south poles of the bubble. As the process continues, more and more of the surface of the bubble participates in the impact process. Before initial impact, the fluid in the re-entrant jet is moving toward the wall with high speed and the fluid on the other side of the bubble is moving away from the wall. The relative velocity of the poles of the bubble at the instant before initial impact increases with increasing Z_0 (the initial distance of the bubble centroid from the wall). During impact, a high-pressure region that is generated around the vortex sheet dramatically decelerates the fluid in the re-entrant jet and forces the fluid on the other side of the bubble to accelerate toward the wall. The impact process generates circulation in the potential flow system. The circulation along a closed path that starts at the north pole, ends at the south pole and encloses both the impact interface and the ring bubble is constant after the initial instant of impact. This circulation increases with decreasing Z_0. Just after initial impact, the source of this circulation is a bound vortex in the ring bubble. However, by the end of the calculation as much as one-half of this total circulation is associated with the vortex sheet. The liquid–liquid impact process results in a loss of energy in the potential flow system. The energy loss increases with

increasing Z_0 and its value at $Z_0 = 1.75$ is about 17% of the total flow energy. In a compressible flow this energy would primarily generate pressure waves. It is thought that in the potential flow system this energy is radiated away suddenly by the infinite sound speed. When Z_0 is small (on the order of the maximum bubble radius), the impact interface forms very close to the wall and the pressure on the wall directly under the bubble increases suddenly upon initial impact. This high-pressure region is quite small in radial extent. As Z_0 increases, the pressure rise at the wall due to impact is spread over a larger area. This may explain the enhanced potential for cavitation erosion with small Z_0 values.

The authors would like to thank Drs Ugo Piomelli and Ramani Duraiswami for a number of useful discussions during this work. Thanks are also due to Dr John Blake for his valuable comments and suggestions during his visit to DYNAFLOW, Inc. in the summer of 1992, and to Dr William Szymczak for helpful discussions concerning the energy losses during impact. S.Z. and J.H.D. acknowledge the support of the state of Maryland and DYNAFLOW, Inc. under a Maryland Industrial Partnerships contract between the University of Maryland and DYNAFLOW, Inc.

Appendix A. Derivations of the integral equations with regular and non-regular surfaces

Let D_i and D_e be defined as the interior and exterior regions, respectively, in a three-dimensional space. An interior boundary dividing D_i and D_e is denoted by S. The field point is represented by $\boldsymbol{p}$ which can be inside D_i or D_e or on S, while the source point, $\boldsymbol{q}$, is on S only. Based on potential theory (Günter 1967; Burton & Miller 1971), the single-layer and double-layer potentials are, respectively,

$$V[\sigma(\boldsymbol{p})] = \int_S G(\boldsymbol{p},\boldsymbol{q})\,\sigma(\boldsymbol{q})\,\mathrm{d}S_q, \tag{A 1}$$

and

$$W[\sigma(\boldsymbol{p})] = \int_S \frac{\partial G(\boldsymbol{p},\boldsymbol{q})}{\partial n_q}\,\sigma(\boldsymbol{q})\,\mathrm{d}S_q, \tag{A 2}$$

where σ is the density function. Assuming that σ is sufficiently continuous on S, as the field point $\boldsymbol{p}$ approaches the boundary S from D_i or D_e, the single-layer potential and the normal derivative of the double-layer potential are continuous across the boundary,

$$V(\sigma)|_S = V(\sigma)|_{int} = V(\sigma)|_{ext}, \tag{A 3}$$

$$\left.\frac{\partial W(\sigma)}{\partial n_p}\right|_S = \left.\frac{\partial W(\sigma)}{\partial n_p}\right|_{int} = \left.\frac{\partial W(\sigma)}{\partial n_p}\right|_{ext}, \tag{A 4}$$

where in (A 3) and (A 4), S, *int* and *ext* subscripts represent the limit values of a function of $\boldsymbol{p}$ for the cases of $\boldsymbol{p}\in S$, $\boldsymbol{p}\to S$ from D_i and $\boldsymbol{p}\to S$ from D_e, respectively, and n_p is the outward normal to S at the field point $\boldsymbol{p}$. However, the double-layer potential and the normal derivative of the single-layer potential are discontinuous as $\boldsymbol{p}$ crosses S. These discontinuities satisfy the following relations:

$$\left.\frac{\partial V(\sigma)}{\partial n_p}\right|_S = \left.\frac{\partial V(\sigma)}{\partial n_p}\right|_{int} - 2\pi\sigma = \left.\frac{\partial V(\sigma)}{\partial n_p}\right|_{ext} + 2\pi\sigma, \tag{A 5}$$

$$W(\sigma)|_S = W(\sigma)|_{int} + 2\pi\sigma = W(\sigma)|_{ext} - 2\pi\sigma. \tag{A 6}$$

According to these fundamental relations, the modified conventional and hypersingular boundary integral equations with common points are derived as follows.

A.1. *Modified CBIE with a common surface*

In view of the fact that the surface S is composed of a regular surface S_b and a common surface $S^+ \cap S^-$ (see figure 1*b*), and on the common surface is imposed

$$\frac{\partial \phi^+(\boldsymbol{p})}{\partial n_p^+} = -\frac{\partial \phi^-(\boldsymbol{p})}{\partial n_p^-},$$

the CBIE (19) can be rewritten as, for $\boldsymbol{p} \in D_i$,

$$4\pi\phi(\boldsymbol{p}) = \int_{S_b}\left[G(\boldsymbol{p},\boldsymbol{q})\frac{\partial\phi(\boldsymbol{q})}{\partial n_q} - \frac{\partial G(\boldsymbol{p},\boldsymbol{q})}{\partial n_q}\phi(\boldsymbol{q})\right]\mathrm{d}S_q - \int_{S^+}\frac{\partial G(\boldsymbol{p},\boldsymbol{q})}{\partial n_q^+}(\phi^+(\boldsymbol{q}) - \phi^-(\boldsymbol{q}))\,\mathrm{d}S_s^+. \quad \text{(A 7)}$$

As $\boldsymbol{p}$ approaches S^+ from D_i, the discontinuity condition (A 6) requires that

$$\int_S \frac{\partial G}{\partial n_q}\phi\,\mathrm{d}S_q\bigg|_{int} = \int_S \frac{\partial G}{\partial n_q}\phi\,\mathrm{d}S_q\bigg|_S - 2\pi\phi. \quad \text{(A 8)}$$

Thus, the integral along S^+ in (A 7) becomes

$$\int_{S^+}\frac{\partial G(\boldsymbol{p},\boldsymbol{q})}{\partial n_q^+}(\phi^+(\boldsymbol{q}) - \phi^-(\boldsymbol{q}))\,\mathrm{d}S_q^+\bigg|_{int} = \int_{S^+}\frac{\partial G(\boldsymbol{p},\boldsymbol{q})}{\partial n_q^+}(\phi^+(\boldsymbol{q}) - \phi^-(\boldsymbol{q}))\,\mathrm{d}S_q^+\bigg|_{S^+} - 2\pi(\phi^+(\boldsymbol{p}) - \phi^-(\boldsymbol{p})). \quad \text{(A 9)}$$

The substitution of (A 9) into (A 7) yields the modified CBIE with a common surface $S^+ \cap S^-$ for $\boldsymbol{p} \in S^+$:

$$2\pi[\phi^+(\boldsymbol{p}) + \phi^-(\boldsymbol{p})] = \int_{S_b}[G(\boldsymbol{p},\boldsymbol{q})\frac{\partial\phi(\boldsymbol{q})}{\partial n_q} - \frac{\partial G(\boldsymbol{p},\boldsymbol{q})}{\partial n_q}\phi(\boldsymbol{q})]\,\mathrm{d}S_q - \int_{S^+}\frac{\partial G(\boldsymbol{p},\boldsymbol{q})}{\partial n_q^+}(\phi^+(\boldsymbol{q}) - \phi^-(\boldsymbol{q}))\,\mathrm{d}S_q^+. \quad \text{(A 10)}$$

For $\boldsymbol{p} \in S_b$, the left-hand side of (A 10) becomes $2\pi\phi(\boldsymbol{p})$ and there is no change on the right-hand side.

A.2. *Modified HBIE with a common surface*

A hypersingular integral equation with a common surface can be derived in a similar fashion. First, the directional differentiation of (A 7) with respect to n_p with $\boldsymbol{p} \in D_i$ yields

$$4\pi\frac{\partial\phi(\boldsymbol{p})}{\partial n_p} = \int_{S_b}\left[\frac{\partial G(\boldsymbol{p},\boldsymbol{q})}{\partial n_p}\frac{\partial\phi(\boldsymbol{q})}{\partial n_q} - \frac{\partial^2 G(\boldsymbol{p},\boldsymbol{q})}{\partial n_p\,\partial n_q}\phi(\boldsymbol{q})\right]\mathrm{d}S_q - \int_{S^+}\frac{\partial^2 G(\boldsymbol{p},\boldsymbol{q})}{\partial n_p\,\partial n_q^+}(\phi^+(\boldsymbol{q}) - \phi^-(\boldsymbol{q}))\,\mathrm{d}S_q^+. \quad \text{(A 11)}$$

Then, let n_p be an outward normal to the boundary S at the inner limit of $\boldsymbol{p}$ on S and pass the limit of $\boldsymbol{p}$ from D_i along the normal n_p to the boundary S. From (A 5), only

the derivative of the single-layer potential, the first integral in (A 11), has a jump according to the relation

$$\int_S \frac{\partial G}{\partial n_p}\frac{\partial \phi}{\partial n_q}\mathrm{d}S_q\bigg|_{int} = \int_S \frac{\partial G}{\partial n_p}\frac{\partial \phi}{\partial n_q}\mathrm{d}S_q\bigg|_S + 2\pi\frac{\partial \phi}{\partial n_p}, \tag{A 12}$$

while the other two integrals along S_b and S^+ in (A 11) are continuous according to (A 4). Thus, (A 11) becomes

$$c_p\frac{\partial \phi(\boldsymbol{p})}{\partial n_p} = \int_{S_b}\left[\frac{\partial G(\boldsymbol{p},\boldsymbol{q})}{\partial n_p}\frac{\partial \phi(\boldsymbol{q})}{\partial n_q} - \frac{\partial^2 G(\boldsymbol{p},\boldsymbol{q})}{\partial n_p\,\partial n_q}\phi(\boldsymbol{q})\right]\mathrm{d}S_q$$

$$-\int_{S^+}\frac{\partial^2 G(\boldsymbol{p},\boldsymbol{q})}{\partial n_p\,\partial n_q}(\phi^+(\boldsymbol{q})-\phi^-(\boldsymbol{q}))\,\mathrm{d}S_q^+, \tag{A 13}$$

where c_p satisfies

$$c_p = \begin{cases} 0, & \boldsymbol{p}\in D_e \\ 2\pi, & \boldsymbol{p}\in S_b \\ 4\pi, & \boldsymbol{p}\in D_i\cup S^+. \end{cases}$$

Appendix B. Derivation of the equation for the energy loss

The first step in the analysis that demonstrates the energy loss due to impact is to take the gradient of the pressure impulse equation (15):

$$\nabla\phi'' = -\nabla I/\rho + \nabla\phi', \tag{B 1}$$

where ϕ' and ϕ'' are the velocity potentials of any point inside the fluid domain at the instants just before and just after the impact, respectively. Next, the difference in the kinetic energy per unit volume before and after the impact, Δe_k, is calculated by squaring (B 1) and rearranging the terms:

$$\Delta e_k = \tfrac{1}{2}\rho(\nabla\phi'')^2 - \tfrac{1}{2}\rho(\nabla\phi')^2 = -\nabla I\cdot\nabla\phi' + (\nabla I)^2/2\rho. \tag{B 2}$$

Since the boundaries of the flow move only an infinitesimal amount over the time of the impulse, the total energy loss is found by integrating e_k over the simply connected volume bounded internally by S_b, S^+ and S^- and externally by S_w and S_∞:

$$\Delta E_k = \int_D e_k\,\mathrm{d}V = \int_D -\nabla I\cdot\nabla\phi'\,\mathrm{d}V + \int_D (\nabla I)^2/2\rho\,\mathrm{d}V. \tag{B 3}$$

The first term on the right-hand side can be manipulated using the chain rule to obtain

$$\int_D \nabla I\cdot\nabla\phi'\,\mathrm{d}V = \int_D \nabla\cdot(I\nabla\phi')\,\mathrm{d}V - \int_D I\nabla^2\phi'\,\mathrm{d}V. \tag{B 4}$$

The last term on the right in this equation is equal to zero since the flow field is incompressible before (and after) impact and D is a simply connected region. Using Gauss's theorem and the fact that $I = 0$ on S_b and S_∞, $\nabla\phi'\cdot\boldsymbol{n}_w = 0$ on S_w, and $\boldsymbol{n}_- = -\boldsymbol{n}_+$ and $I^+ = I^-$ on the common surface, the first term on the right of (B 3) can be written as

$$\int_D \nabla I\cdot\nabla\phi'\,\mathrm{d}V = \int_{S^+} I^+(\nabla(\phi')^+ - \nabla(\phi')^-)\cdot\boldsymbol{n}_+\,\mathrm{d}S. \tag{B 5}$$

The second term on the right of (B 3) can be manipulated in a similar manner. First, the chain rule is used to obtain

$$\int_D (\nabla I)^2 \,\mathrm{d}V = \int_D \nabla\cdot(I\nabla I)\,\mathrm{d}V - \int_D I\nabla^2 I\,\mathrm{d}V. \tag{B 6}$$

The second term on the right of this equation is equal to zero since the Laplacian of the pressure impulse is zero in D, as can be seen by taking the divergence of (B 1). Using Gauss's theorem, and the conditions $I = 0$ on S_∞ and S_b,

$$\nabla I\cdot\boldsymbol{n}_w = \rho(\nabla\phi'\cdot\boldsymbol{n}_w - \nabla\phi''\cdot\boldsymbol{n}_w) = 0 \text{ on } S_w$$

(see (B 1)), and $I^+ = I^-$ and $\boldsymbol{n}_- = -\boldsymbol{n}_+$ on the common surface, the first term on the right of (B 6) can be written

$$\int_D \nabla\cdot(I\nabla I)\,\mathrm{d}V = \int_{S^+} I^+(\nabla I^+ - \nabla I^-)\cdot\boldsymbol{n}_+\,\mathrm{d}S. \tag{B 7}$$

This last integral can be further manipulated using (B 1) and the matching condition on the common surface (8) just after impact to obtain

$$\int_D \nabla\cdot(I\nabla I)\,\mathrm{d}V = \rho\int_{S^+} I^+(\nabla(\phi')^+ - \nabla(\phi')^-)\cdot\boldsymbol{n}_+\,\mathrm{d}S. \tag{B 8}$$

Finally, plugging (B 5) and (B 8) into (B 3) the equation for the change in kinetic energy is obtained:

$$\Delta E_k = -\frac{1}{2}\int_{S^+} I^+(\nabla(\phi')^+ - \nabla(\phi')^-)\cdot\boldsymbol{n}_+\,\mathrm{d}S. \tag{B 9}$$

Appendix C. Representation of the hypersingular integral equations in terms of elliptical integrals

Assume a cylindrical coordinate system (r, θ, z), and let the three unit vectors in the r-, θ- and z-directions be denoted by $\boldsymbol{e}_r$, $\boldsymbol{e}_\theta$ and $\boldsymbol{e}_z$, respectively. Assume that both the source point $\boldsymbol{q}(r_q, \theta_q, z_q)$ and the field point $\boldsymbol{p}(r_p, \theta_p, z_p)$ are on the surface S_b and that $\theta_p = 0$. Since the problem is axisymmetric about the z-axis, the two unit vectors representing the outward normals to S_b at $\boldsymbol{p}$ and $\boldsymbol{q}$ are given by $\boldsymbol{n}_p(\sin\alpha_p, 0, \cos\alpha_p)$ and $\boldsymbol{n}_q(\sin\alpha_q, 0, \cos\alpha_q)$, respectively, where α_p (or α_q) is the angle between $\boldsymbol{n}_p$ (or $\boldsymbol{n}_q$) and the positive r-direction. With the above assumptions and definitions, (28) can be written as

$$\begin{aligned}\int_S \phi(\boldsymbol{q})\frac{\partial^2 G(\boldsymbol{p},\boldsymbol{q})}{\partial\boldsymbol{n}_p\,\partial\boldsymbol{n}_q}\,\mathrm{d}S_q &= \int_S [\boldsymbol{n}_q\times\nabla_q\phi(\boldsymbol{q})]\cdot[\boldsymbol{n}_p\times\nabla_p G(\boldsymbol{p},\boldsymbol{q})]\,\mathrm{d}S_q \\ &= \int_S\left[\sin\alpha_p\frac{\partial(G\cos\theta_q)}{\partial r_p} - \cos\alpha_p\frac{\partial(G\cos\theta_q)}{\partial z_p}\right]\frac{\partial\phi}{\partial s_q}\,\mathrm{d}S_q.\end{aligned} \tag{C 1}$$

The above equation can also be written as

$$\int_S \phi(\boldsymbol{q})\frac{\partial^2 G(\boldsymbol{p},\boldsymbol{q})}{\partial\boldsymbol{n}_p\,\partial\boldsymbol{n}_q}\,\mathrm{d}S_q = \int_S\left[-\sin\alpha_p\frac{\partial G}{\partial r_q} + \cos\alpha_p\frac{\partial(G\cos\theta_q)}{\partial z_q}\right]\frac{\partial\phi}{\partial s_q}\,\mathrm{d}S_q \tag{C 2}$$

by using the relation $\nabla_p G(\boldsymbol{p},\boldsymbol{q}) = -\nabla_q G(\boldsymbol{p},\boldsymbol{q})$. This latter equation is easier to treat than (C 1) as $r_p \to 0$.

The integral equations in §2 can be integrated analytically in the θ-direction and represented in terms of elliptical integrals. Introducing the elliptical integrals of the first kind $K(m)$ and the second kind $E(m)$ as

$$K(m) = \int_0^{\pi/2} \frac{\mathrm{d}\beta}{(1-m^2\sin\beta)^{\frac{1}{2}}}, \tag{C 3}$$

$$E(m) = \int_0^{\pi/2} (1-m^2\sin\beta)^{\frac{1}{2}}\,\mathrm{d}\beta, \tag{C 4}$$

where $m^2 = 4r_p r_q/A$ and $A = (r_p+r_q)^2+(z_p-z_q)^2$, the terms resulting from the θ-integrations in (21) are

$$I_1 = 4K(m)/A^{\frac{1}{2}}, \tag{C 5}$$

$$I_2 = [8(K(m)-E(m))/m^2-4K(m)]/A^{\frac{1}{2}}. \tag{C 6}$$

Substituting these relations into (19) and (21) yields

$$c_p\phi(p) = \int_L \left[C_{pq}\frac{\partial\phi(q)}{\partial n_q}+D_{pq}\phi(q)\right]\mathrm{d}L_q, \tag{C 7}$$

$$c_p\frac{\partial\phi(p)}{\partial n_p} = \int_L \left[E_{pq}\frac{\partial\phi(q)}{\partial n_q}+F_{pq}\frac{\partial\phi(q)}{\partial s_q}\right]\mathrm{d}L_q, \tag{C 8}$$

where L is an intersection curve between S_b and the plane $\theta = 0$, and

$$C_{pq} = r_q I_1, \tag{C 9}$$

$$D_{pq} = -r_q\,\partial I_1/\partial n_q, \tag{C 10}$$

$$E_{pq} = r_q\,\partial I_1/\partial n_p, \tag{C 11}$$

$$F_{pq} = -r_q(-\sin\alpha_p\,\partial I_1/\partial r_q+\cos\alpha_p\,\partial I_2/\partial z_q). \tag{C 12}$$

With the relations

$$\frac{\mathrm{d}K(m)}{\mathrm{d}m} = \frac{1}{m}\left(\frac{E(m)}{1-m^2}-K(m)\right), \tag{C 13}$$

$$\frac{\mathrm{d}E(m)}{\mathrm{d}m} = \frac{E(m)-K(m)}{m}, \tag{C 14}$$

the partial derivatives of I_1 and I_2 needed to calculate D_{pq}, E_{pq} and F_{pq} can be expressed as follows

$$\frac{\partial I_1}{\partial r_q} = \frac{4(r_p-r_q)\,E(m)}{A^{\frac{3}{2}}(1-m^2)}-\frac{2(K(m)-E(m))}{A^{\frac{1}{2}}r_q}, \tag{C 15}$$

$$\frac{\partial I_1}{\partial z_q} = \frac{4(z_p-z_q)\,E(m)}{A^{\frac{3}{2}}(1-m^2)}, \tag{C 16}$$

$$\frac{\partial I_1}{\partial r_p} = -\frac{4(r_p-r_q)\,E(m)}{A^{\frac{3}{2}}(1-m^2)}-\frac{2(K(m)-E(m))}{A^{\frac{1}{2}}r_p}, \tag{C 17}$$

$$\frac{\partial I_1}{\partial z_p} = -\frac{4(z_p-z_q)\,E(m)}{A^{\frac{3}{2}}(1-m^2)}, \tag{C 18}$$

$$\frac{\partial I_2}{\partial z_q} = -\frac{8(z_p-z_q)(K(m)-E(m))}{A^{\frac{3}{2}}m^2}+\frac{4(z_p-z_q)\,E(m)}{A^{\frac{3}{2}}(1-m^2)}. \tag{C 19}$$

REFERENCES

ANDERSON, D. C. 1965 Gaussian quadrature formulae for $-\int_0^1 \ln(x) f(x)\,dx$. *Math. Comput.* **19**, 477–481.

ARNDT, R. E. 1981 Recent advances in cavitation research. *Adv. Hydrosci.* **12**, 1–78.

BATCHELOR, G. K. 1967 *An Introduction to Fluid Dynamics*. Cambridge University Press.

BENJAMIN, T. B. & ELLIS, A. T. 1966 The collapse of cavitation bubbles and the pressures thereby produced against solid boundaries. *Phil. Trans. R. Soc. Lond.* A **260**, 221–240.

BEST, J. 1993 The formation of toroidal bubbles upon the collapse of transient cavities. *J. Fluid Mech.* **251**, 79–107.

BEVIR, M. K. & FIELDING, P. J. 1974 Numerical solution of incompressible bubble collapse with jetting. In *Moving Boundary Problems in Heat Flow and Diffusion* (ed. J. R. Ockendon & W. R. Hodgkins). Clarendon.

BLAKE, J. R. & GIBSON, D. C. 1981 Growth and collapse of a vapour cavity near a free surface. *J. Fluid Mech.* **111**, 123–140.

BLAKE, J. R. & GIBSON, D. C. 1987 Cavitation bubbles near boundaries. *Ann. Rev. Fluid Mech.* **19**, 99–123.

BLAKE, J. R., TAIB, B. B. & DOHERTY, G. 1986 Transient cavities near boundaries. Part 1. Rigid boundary. *J. Fluid Mech.* **170**, 474–497.

BURTON, A. J. & MILLER, G. F. 1971 The application of integral equation methods to the numerical solution of some exterior boundary-value problems. *Proc. R. Soc. Lond.* A **323**, 201–210.

CERONE, P. & BLAKE, J. R. 1984 A note on the instantaneous streamlines, pathlines and pressure contours for a cavitation bubble near a rigid boundary. *J. Austral. Math. Soc.* B **26**, 31–44.

CHAHINE, G. L. 1979 Etude locale du phénomène de cavitation – analyses des facteurs régissant la dynamique des interfaces. Doctorat D'Etat Es-Sciences Thesis, Université Pierre et Marie Curie.

CHAHINE, G. L. 1982 Experimental and asymptotic study of nonspherical bubble collapse. *Appl. Sci. Res.* **38**, 187–197.

CHAHINE, G. L. 1991 Dynamics of the interaction of non-spherical cavities. In *Mathematical Approaches in Hydrodynamics* (ed. T. Miloh). SIAM.

CHAHINE, G. L. & PERDUE, T. O. 1988 Simulation of the three-dimensional behavior of an unsteady large bubble near a structure. In *Drops and Bubbles, Third Intl Colloq., Monterey, CA* (ed. T. G. Wang), pp. 188–199. American Institute of Physics.

DOMMERMUTH, D. G. & YUE, D. K. P. 1987 Numerical simulations of nonlinear axisymmetric flows with a free surface. *J. Fluid Mech.* **178**, 195–219.

DUNCAN, J. H. & ZHANG, S. 1991 On the interaction of a collapsing cavity and a compliant wall. *J. Fluid Mech.* **226**, 401–423.

GIBSON, D. C. 1968 Cavitation adjacent to plane boundaries. *Proc. 3rd Austral. Conf. on Hydraulics and Fluid Mech.*, pp. 210–214. Institution of Engineers, Sydney, Australia.

GIBSON, D. C. & BLAKE, J. R. 1980 Growth and collapse of cavitation bubble near flexible boundaries. *Proc. 7th Austral. Hydraulics and Fluid Mech. Conf., Brisbane*, pp. 283–286. Institution of Engineers, Sydney, Australia.

GIBSON, D. C. & BLAKE, J. R. 1982 The growth and collapse and bubbles near deformable surfaces. *Appl. Sci. Res.* **28**, 215–224.

GUERRI, L., LUCCA, G. & PROSPERETTI, A. 1981 A numerical method for the dynamics of non-spherical cavitation bubbles. *Proc. 2nd Intl Colloq. on Drops and Bubbles, California*, pp. 175–181.

GÜNTER, N. M. 1956 *Potential Theory and Its Application to Basic Problems of Mathematical Physics*. Frederick Ungar.

HAMMITT, F. G. 1980 *Cavitation and Multiphase Flow Phenomena*. McGraw-Hill.

INGBER, M. S. & RUDOLPHI, T. J. 1990 Solution of potential problems using combinations of the regular and derivative boundary integral equations. *Appl. Math. Modeling* **14**, 536–543.

KELLOGG, O. D. 1953 *Foundations of Potential Theory*. Dover.

KRISHNASAMY, G., SCHMERR, L. W., RUDOLPHI, T. J. & RIZZO, F. J. 1990 Hypersingular boundary integral equations: some applications in acoustic and elastic wave scattering. *Trans. ASME* E: *J. Appl. Mech.* **57**, 404–414.

LAMB, H. 1945 *Hydrodynamics*. Dover.

LAUTERBORN, W. & BOLLE, H. 1975 Experimental investigations of cavitation-bubble collpase in the neighbourhood of a solid boundary. *J. Fluid Mech.* **72**, 391–399.

LONGUET-HIGGINS, M. S. & COKELET, E. D. 1976 The deformation of steep surface waves in water, I. A numerical method of computation. *Proc. R. Soc. Lond.* A **350**, 1–26.

LUNDGREN, T. S. & MANSOUR, N. N. 1991 Vortex ring bubbles. *J. Fluid Mech.* **224**, 177–196.

MATHEMATICAL HANDBOOK EDITORIAL GROUP 1977 Mathematical Handbook. Beijing: Higher Education Publications (in Chinese).

MEYER, W. L., BELL, W. A. & ZINN, B. T. 1978 Boundary integral solutions of three dimensional acoustics radiation problems. *J. Sound Vib.* **59**, 245–262.

MITCHELL, T. M. & HAMMITT, F. G. 1973 Axisymmetric cavitation bubble collapse. *Trans. ASME* I: *J. Fluids Engng* **95**, 29–37.

MOON, P. & SPENCEL, D. E. 1961 *Field Theory Handbook*. Springer.

OĞUZ, H. N. & PROSPERETTI, A. 1990 Bubble entrainment by the impact of drops on liquid surfaces. *J. Fluid Mech.* **219**, 143–159.

PLESSET, M. S. & CHAPMAN, R. B. 1971 Collapse of an initially spherical vapour cavity in the neighbourhood of solid boundary. *J. Fluid Mech.* **47**, 283–290.

PRESS, H. W., FLANNERY, B. P., TENKOLSKY, S. A. & VETTELING, W. T. 1989 *Numerical Recipes*. Cambridge University Press.

PROSPERETTI, A. 1982 Bubble dynamics: a review and some recent results. *Appl. Sci. Res.* **38**, 145–164.

RAYLEIGH, LORD 1917 On the pressure developed in a liquid during the collapse of a spherical void. *Phil. Mag.* **34**, 94–98.

ROGERS, J. C. W., SZYMCZAK, W. G., BERGER, A. E. & SOLOMON, J. M. 1990 Numerical solution of hydrodynamic free boundary problems. *Intl Series Numer. Maths* **95**, 241–266.

SHIMA, A., TOMITA, Y., GIBSON, D. C. & BLAKE, J. R. 1989 The growth and collapse of cavitation bubbles near composition surfaces. *J. Fluid Mech.* **203**, 199–214.

SZYMCZAK, W. G., ROGERS, J. C. W., SOLOMON, J. M. & BERGER, A. E. 1993 A numerical algorithm for hydrodynamic free boundary problems. *J. Comput. Phys.* **106**, 319–336.

TOMITA, Y. & SHIMA, A. 1986 Mechanisms of impulsive pressure generation and damage pit formation by bubble collapse. *J. Fluid Mech.* **169**, 535–564.

VOGEL, A., LAUTERBORN, W. & TIMM, R. 1989 Optical and acoustic investigations of the dynamics of laser-produced cavitation bubbles near a solid boundary. *J. Fluid Mech.* **206**, 299–338.